Master's Degree in Mechanical Engineering

Numerical and Data-Driven Modeling of an Impact Test Facility for Pyroshock Qualification

Development and Validation of Contact Mechanics Models

Politecnico di Torino

Supervisors:
Prof. Alessandro Fasana
Prof. Luca Viale

Candidate:
Riccardo Fracasso

Academic Year 2024 / 2025

To my loving family, for the unwavering support and belief in me;
and to Alice, for her constant encouragement, and love.

Acknowledgements

I would like to express my sincere gratitude to my supervisors, Ing. Luca Viale and Prof. Alessandro Fasana, for their invaluable guidance, support, and encouragement throughout the development of this thesis.

Their expertise and constant support were instrumental in helping me overcome the challenges encountered along the way. Their mentorship has played a fundamental role in both my academic and personal growth, and I am truly grateful for the opportunity to have worked under their supervision.

I am also deeply thankful to my family and my girlfriend for their unwavering support, patience, and encouragement throughout this journey. Their presence and understanding have been a continuous source of strength and motivation during my studies.

Abstract

During aerospace missions, payloads and subsystems endure extreme dynamic loads. Pyrotechnic devices, such as those used for stage separation, secondary structure deployment, or appendage release, produce high-energy transients known as pyroshocks. These pyroshocks pose a significant threat to electronic components and can compromise the success of the mission. Qualifying hardware therefore demands pyroshock testing, typically performed by striking resonant plates with projectiles or hammers to reproduce the shock response spectrum prescribed in standards. Because these tests rely on iterative, empirical tuning, experimental qualification remains time consuming and cost intensive.

State of the art numerical methods can shorten this process by predicting the responses of resonant plates, but their accuracy hinges on correctly modelling impact forces and contact durations, which govern the resulting spectral content. After reviewing contact mechanics and current experimental configurations, this thesis develops a data-driven ML contact model and a numerical impact velocity predictor that couples with a pre-existing finite element model of the plate to form a complete digital twin of a pyroshock test bench. Validation against experimental data shows that these models achieve high fidelity in force,timing and velocity prediction, indicating strong potential to reduce calibration cycles and diminish qualification costs.

Lastly the pyroschock testing facility at Politecnico di Torino is finalized with the dimensioning of the suspension components used for the plate and a proposal for the design af a safety plate to place behind the resonant one. The experimental setup is accompanied by the conceptualization of the complete measurement chain capable of acquiring the data needed to rigorously validate the digital twin and to study parameter sensitivity in shock testing, laying the groundwork for more efficient, repeatable, and cost-effective pyroshock qualification tests.

Contents

List of Figures vii

List of Tables x

Nomenclature xii

1 Introduction 1

1.1 Pyroshock test benches 5

1.2 Impact overview 9

1.2.1 Continuous Approach 12

1.2.2 Data-Driven Models 16

1.3 Objectives 18

2 Experimental Setup 20

2.1 Components 20

2.1.1 Frame and resonant plate 20

2.1.2 Pneumatic Gun 24

2.1.3 Safety plate 27

2.2 Sensors and acquisition 30

2.2.1 Sensors 30

2.2.2 Acquisition 35

2.3 Impacting velocity prediction 35

3 Preliminary tests and Design of Experiments 39

3.1 Preliminary tests 39

3.2 Complete Design of Experiments 40

4 Contact Mechanics 43

4.1 Processing of the database 45

4.2 Selection of Inputs and Outputs of the models 52

4.2.1 Inputs 52

4.2.2 Outputs 54

4.3 Models 56

4.3.1 Contact time prediction 57

4.3.2 Force prediction 57

4.4 Optimization 61

5 Results 65

5.1 Validation of velocity prediction model 65

5.2 Contact force estimation 68

6 Conclusions 76

6.1 Future directions 78

Appendix A Latin Hypercube Sampling Dataset 79

References 84

List of Figures

1.1 Graphical representation of SRS construction 4

1.2 Ordnance pyroshock test 6

1.4 Out Of Plane Impact Pendulum 7

1.3 Bounded Impact Shock Machine 7

1.5 Mechanical Impulse Pyroshock Simulator 8

1.6 Electrodynamic Shaker exciter 9

1.7 Force profile obtained by Hunter, Reed and asymmetric von Hann Models. Obtained with a COR of 2/3 16

2.1 Suspension frame and resonant plate 22

2.2 Dimensions of the resonant plate 23

2.3 Pneumatic gun 25

2.4 Pneumatic Circuit of the pneumatic gun, A: compressor, B: pressure regulator, C: manual ball valve, D: digital and analog manometer, E: tank, F: pneumatic ball valve, G: barrel 26

2.5 Modular bullet design: (a) interchangeable bullet tips; (b) bullet main body 27

2.6 Ballistic limit velocity for a 1 kg aluminum projectile (d=48 mm) impacting an aluminum plate. 28

2.7 Ballistic limit velocity for a 1 kg aluminum projectile (d=48 mm) impacting a steel plate. 29

2.8 Measurement chain 30

2.9 Comparison between force measured by a load cell and computed though acceleration 32

2.10 Load cell array (a) Side view, from left to right: plate on which the impact take place, load cells, resonant plate (b) 33

2.11 Scheme of the pneumatic gun model 36

2.12 Mass and pressure influence on exit velocity 38

4.1 Overview of the methodology 43

4.2 Effect of the deconvolution on the acceleration signal in time domain for a randomly selected impact 46

4.3 Proposed methods to isolate the information contained in the experimentally acquired time series 47

4.4 NRMSE between acquired force signal and interpolated one 49

4.5 Difference between the experimentally acquired and interpolated force signal, three randomly selected impacts each with different materials 50

4.6 Perceptual differences in contact duration due to different extraction methods 51

4.7 Comparison of automatic and manual extraction - Test number 1 . . 52

4.8 Correlation between the inputs of the ML models 54

4.9 Steps of the machine learning algorithm to find force evolution in time domain 56

4.10 NRMSE comparison of each of the considered force regression models. From the top: bilayer, trilayer neural networks, narrow, medium, wide neural networks, multivariate linear regression, partial least square regression, gaussian process, support vector regression, support vector machine kernel, kernel regression. 60

5.1 Measured pressure evolution for test 2. The laser signal is used directly in volts since only passage time is needed and not the distance of the object. 67

5.2 Comparison of numerical velocity model and actual measurements . 68

5.3 Colormap of the proposed cost function with a generic pulse and relative tolerances. 70

5.4 Cost function computed for each test 72

5.5 Error on impulse of each test 75

List of Tables

2.1 Components used to suspend the plate and relative safety factor . . . 24

3.1 Tank pressure and measured exit velocity for five low pressure tests 40

3.2 Controllable variables and their levels for the DOE 41

4.1 Experimental factor levels 44

4.2 Material properties used in the study 45

4.3 Predictor chosen as inputs for the machine learning models 53

4.4 RMSE for each time prediction model 57

4.5 Mean RMSE and NRMSE of each force regression model 61

4.6 Optimized Hyperparameters Gaussian Process for Time prediction in GPyTorch 63

4.7 Optimized Hyperparameters Gaussian Process for Force prediction in GPyTorch 63

4.8 Optimized Hyperparameters Gaussian Process for Time prediction - MATLAB 63

4.9 Optimized Hyperparameters Neural Network Force prediction - MATLAB 64

5.1 Comparison of predicted and measured bullet velocities, uncertainties in are computed via Eq. 5.2 66

5.2 Mean cost value and RMSE over the entire dataset of each prediction model 71

5.3 Mean errors between predictions and acquired signals on key physical parameters 73

A.1 LHS Design of Experiments 80

Nomenclature

Greek Symbols

δ	Displacement
λ	Zener's Inelasticity factor
ν	Poisson's Ratio
ρ	Density
σ_y	Yielding Strenght
τ	Contact Time
ζ	Damping Ratio

Subscripts

an	Referring to Anelastic Restitution
c	Referring to Compression
el	Referring to Elastic Compression Phase
i	Referring to Initial State before the Impact
max	Referring to Maximum Value
p	Referring to Impacting Plate
r	Referring to Restitution
s	Referring to Impacting Sphere or Bullet

Other Symbols

a	Acceleration
E	Young's Modulus
e	Coefficient Of Restitution
F	Contact Force
K	Kernel Function
k	Contact Stiffness
m	Mass
R	Curvature Radius
T_s	Sampling period
u	Impacting Object speed
u_{bl}	Ballistic Limit Velocity
P	Impulse
W	Work

Acronyms / Abbreviations

BCs	Boundary Conditions
COR	Coefficient Of Restitution
DOE	Design Of Experiments
GA	Genetic Algorithm
GPR	Gaussian Process Regresssion
GUM	Guide to the Expression of Uncertainty in Measurement
ifft	Inverse Fast Fourier Transform
LHS	Latin Hypercube Sampling

MIPS Mechanical Impulse Pyroshock Simulator

NNs Neural Networks

NRMSE Normalized Root Mean Square Error

ODE Ordinary Differential Equation

OVAT One Variable At a Time

PLA Polylactic Acid polymer

PLS Partial Least Squares

ReLU Rectified Linear Unit

RMSE Root Mean Square Error

SDOF Single Degree of Freedom

SF Safety Factor

SRS Shock Response Spectrum

SVM Support Vector Machines

tf Transfer Function

Chapter 1

Introduction

In the aerospace sector, explosive charges are widely used to separate stages, release substructures, or deploy appendages during missions. While these methods ensure rapid and precise actuation, they also generate intense transient mechanical loads across the spacecraft. These high-frequency, high-amplitude phenomena, known as pyroshocks, pose a significant threat to the integrity of sensitive onboard components.

Materials most susceptible to pyroshock induced damage include crystals, ceramics, epoxies, glass envelopes, fine wires, and microelectronics, potentially leading to catastrophic mission failures [1]. Direct pyroshock testing on spacecraft structures would yield the most accurate understanding of such loads, but is typically infeasible due to the uniqueness of flight hardware and the need for validation long before integration. Consequently, surrogate methods such as resonant plate testing are used to replicate the spectral content and magnitude of pyroshock events.

According to NASA-STD-7003 [2], pyroshock environments are categorized as follows:

- **Near-field environment**: Direct exposure to the explosive event, with accelerations exceeding 10000 g and dominant frequencies above 10 kHz. Ideally no sensitive components should be mounted in this region.
- **Mid-field environment**: Characterized by combined wave propagation and structural resonances, with accelerations between 1000–10000 g and frequency content in the 3–10 kHz range.

- **Far-field environment**: dominated by structural resonances, with accelerations limited to less than 1000g and the majority of the spectrum below 3 kHz

Shocks are typically measured in time domain using accelerometers and, for easier comparison of severity and frequency content, the Shock Response Spectrum (SRS) is used.

The SRS, as defined by ISO 18431-4 [3], represents the maximum response of a set of single degree of freedom (SDOF) mass-damper-spring systems when subjected to a given acceleration input as illustrated in Figure 1.1. The acceleration is applied to the base of each oscillator, and the spectrum is constructed from the maximum responses versus the natural frequency of the oscillators using a conventional damping value $\zeta = 5\%$. While this method facilitates standardization and comparison, it inherently discards critical information such as signal duration and phase. The response of each of the SDOF can be computed in many different ways, analytically the convolution integral can be used:

$$\ddot{y}(t) = \int_0^t \ddot{x}(\tau) h(t-\tau) d\tau \tag{1.1}$$

Where $\ddot{x}(\tau)$ is the generic input and h is the impulse response function. While effective this approach is computationally heavy, so ISO 18431 provides a way of using digital filters to significantly reduce this burden. It starts from the transfer function of a single degree of freedom system when excited by an acceleration.

$$G(s) = \frac{\ddot{y}(s)}{\ddot{x}(s)} = \frac{cs+k}{ms^2+cs+k} \tag{1.2}$$

To replace this continuous transfer function the norm adopts a digital filter that limits at a minimum frequency distortion.

$$H(z) = \frac{\beta_0 + \beta_1 z^{-1} + \beta_2 z^{-2}}{1 + \alpha_1 z^{-1} + \alpha_2 z^{-2}} \tag{1.3}$$

Coefficients β are dependent on which type of response is needed, such as acceleration response or velocity response, while α coefficients are always the same. Both

are defined in the technical standards, in the case of acceleration response:

$$\beta_0 = 1 - e^{-\frac{\omega_n T}{2Q}} \cdot \frac{\sin\left(\omega_n \Delta t \sqrt{1 - \frac{1}{4Q^2}}\right)}{\omega_n \Delta t \sqrt{1 - \frac{1}{4Q^2}}} \tag{1.4}$$

$$\beta_1 = 2e^{-\frac{\omega_n \Delta t}{2Q}} \cdot \left[\frac{\sin\left(\omega_n \Delta t \sqrt{1 - \frac{1}{4Q^2}}\right)}{\omega_n \Delta t \sqrt{1 - \frac{1}{4Q^2}}} - \cos\left(\omega_n \Delta t \sqrt{1 - \frac{1}{4Q^2}}\right) \right] \tag{1.5}$$

$$\beta_2 = e^{-2\frac{\omega_n \Delta t}{2Q}} - e^{-\frac{\omega_n \Delta t}{2Q}} \cdot \frac{\sin\left(\omega_n \Delta t \sqrt{1 - \frac{1}{4Q^2}}\right)}{\omega_n \Delta t \sqrt{1 - \frac{1}{4Q^2}}} \tag{1.6}$$

$$a_1 = -2e^{-\frac{\omega_n \Delta t}{2Q}} \cdot \cos\left(\omega_n \Delta t \sqrt{1 - \frac{1}{4Q^2}}\right) \tag{1.7}$$

$$a_2 = e^{-2\frac{\omega_n \Delta t}{2Q}} \tag{1.8}$$

where:
- $\omega_n = \sqrt{\frac{k}{m}}$ is the natural frequency of an undamped SDOF system
- $\omega_d = \omega_n \sqrt{1 - \zeta^2}$ is the damped natural frequency of a SDOF system
- ζ is the conventional damping coefficient
- $\Delta t = \frac{1}{f_s}$ is the temporal resolution
- $Q = \frac{1}{2\zeta}$ is the damping factor

The normative also prescribes a recommended frequency resolution of 6 samples per octave while computing the response using $\zeta = 5\%$. The resolution can be finer if the damping is reduced in order to capture the sharper response better. A qualitative representation of the creation of a SRS is schematized in Figure 1.1.

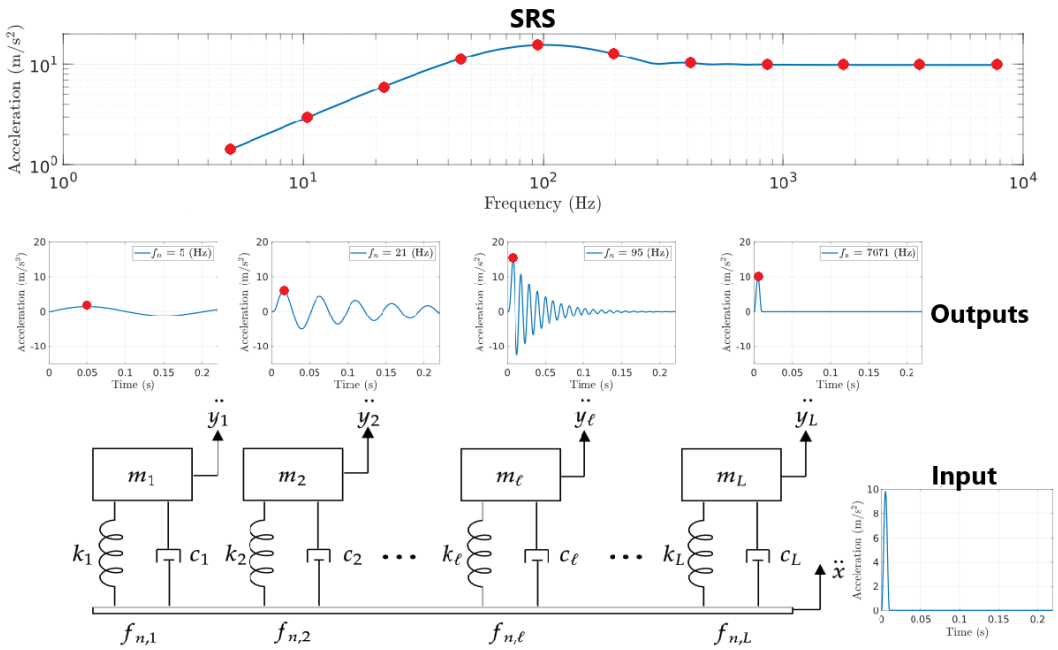

Fig. 1.1 Graphical representation of SRS construction

At Politecnico di Torino a test bench has been designed [4] to use a compressed air cannon to provide excitation to a resonant plate via bullet impacts. This method was chosen over explosive charges to enhance repeatability and improve safety during testing. To optimize the testing procedure, reduce calibration time and costs of the campaigns a digital twin model of the system was developed. The model consists of three main components:

1. Resonant plate: simulated using a Finite Element Method (FEM) model, which incorporates geometry, material properties, and Boundary Conditions (BCs) to predict the plate Frequency Response Function (FRF).

2. Gas launcher: modeled as a finite volume air tank connected to a barrel through a valve. The exit velocity of the projectile is estimated using the dynamics of the projectile and adiabatic expansion.

3. Contact pulse: modeled using a Von Hann window to approximate the shape and duration of the contact force.

A critical aspect of accurately simulating pyroshock is the definition of the contact impulse. Even small variations in pulse shape or duration can alter the resulting spectral content, directly affecting component response.

In this Chapter an overview of pyroshock phenomena, experimental methods, and impact modeling approaches is presented to provide the necessary background before introducing the proposed methodologies in the following Chapters.

1.1 Pyroshock test benches

Over the years, a wide range of excitation methods have been developed for pyroshock testing, which can be broadly classified into main categories: those that utilize explosive charges, those that rely on mechanical pulse generation and non contact methods.

Explosive based techniques represent the most traditional approach to pyroshock testing. These tests often employ the same pyrotechnic devices used in actual aerospace systems. Common devices include explosive bolts and explosive nuts, which are engineered to fracture upon detonation and release mechanical energy. Configurations utilizing explosive bolts and nuts are widely documented in the literature [5, 6]. These methods come with significant safety hazards, are non reusable, and are generally more costly and time consuming. However, when components sensitive to pyroshock are located in near-field environments, standards such as [2] require testing to be conducted in flight-like configurations, making explosive based setups the preferred choice. The usual process is to perform tests on different scales until full scale is, ideally, achieved [7].
The typical sequence begins with an *ordnance test*, where a flexible linear charge is used as shown in Figure 1.2. The correct charge configuration is often optimized by trial-and-error by adjusting parameters such as padding layers between the charge and test article. These tests are initially performed on dummy components to avoid damaging actual hardware, making the process both expensive and time consuming.

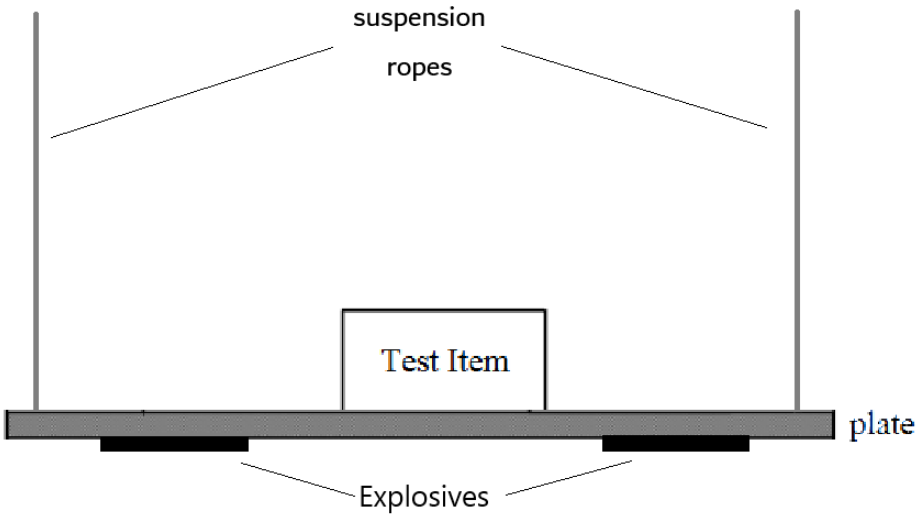

Fig. 1.2 Ordnance pyroshock test

This is followed by a *scaled test*, where explosive bolts or nuts are used to reproduce the expected frequency content in a scaled down but more representative configuration.
Lastly, if the final configuration is particularly complex a *full-scale test* may be required, but this occasion is rare.

The standard also allows for high acceleration mechanical impacts if it can be demonstrated that the resulting shock response spectrum is equivalent to that of a real pyrotechnic event, motivating the development of mechanical alternatives. **Mechanical methods** offer safer, more repeatable, and more controllable means of generating pyroshock-like events. Among the most commonly used mechanical systems is the pendulum impactor, which consists of a rigid arm with a ball head that swings to strike a resonant structure. The impact energy is governed by the pendulum potential energy, which can be tuned by adjusting its initial angular position and the mass of the impacting head. Another widely used method is the bounded impact shock test machine, where a drop table impacts a spring connected fixture. Energy is adjusted by tuning the drop height, mass, and the stiffness/damping of the springs. These setups typically produce sinusoidal like shocks with peak accelerations up to 5000 g and frequencies reaching 2 kHz [8].

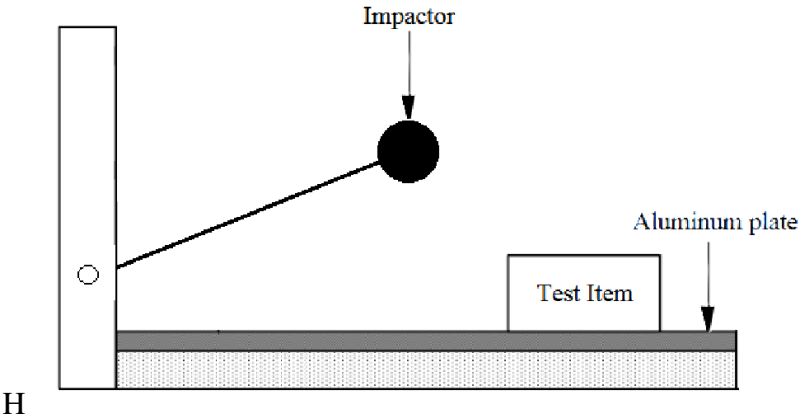

Fig. 1.4 Out Of Plane Impact Pendulum

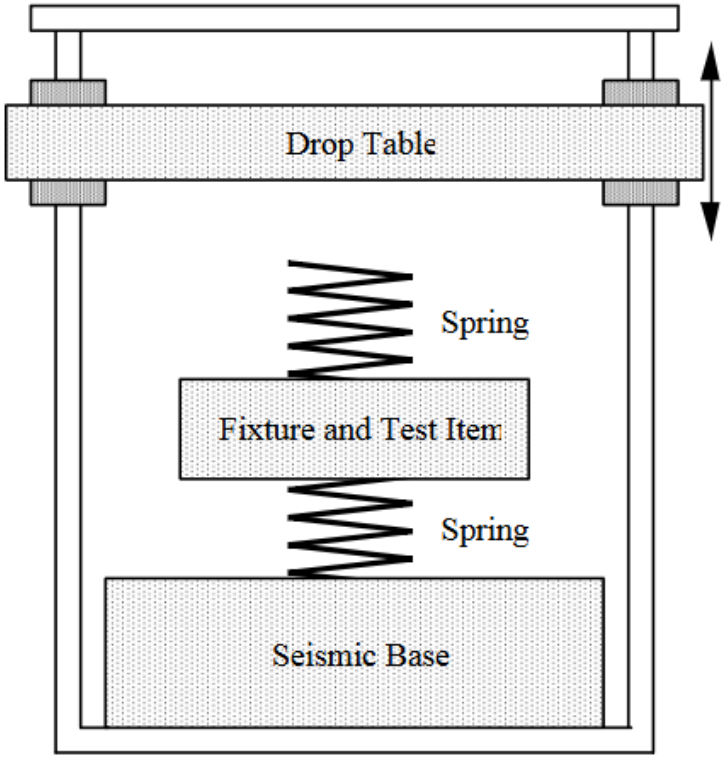

Fig. 1.3 Bounded Impact Shock Machine

A key challenge in both systems is avoiding secondary impacts due to rebound. This requires careful design, such as mechanisms to stop the impacting mass after initial contact. Both in-plane and out-of-plane impacts can be implemented. In-

plane impacts involve excitation in the same plane as the primary structural mode of interest, making them suitable for simulating planar shock propagation. Out-of-plane impacts, on the other hand, strike the structure from an orthogonal direction, often exciting bending or torsional modes that are otherwise difficult to activate. Both configurations have been successfully used in laboratory settings [9, 10] and commercially.

An alternative is the compressed gas projectile system, in which pressurized air or nitrogen accelerates a projectile down a barrel to strike the test item or a resonant fixture [11]. These systems have lower susceptibility to secondary impacts compared to pendulums. Notably, facilities like Sandia National Laboratories [12] have developed large scale systems capable of launching projectiles up to 45 kg through 18 meter barrels, achieving highly controlled and powerful impacts. By tuning barrel length, pressure level, and projectile mass and the shape of the fixture and resonant component, the impact energy and shock spectrum can be finely controlled to match target specifications.
A variation of this principle is the Mechanical Impulse Pyroshock Simulator (MIPS), where a pneumatic actuator mounted on a gantry drives an end effector into the test fixture instead of a bullet. While limited to mid-field environments (up to 5000 g, 10 kHz), MIPS systems offer excellent repeatability [7].

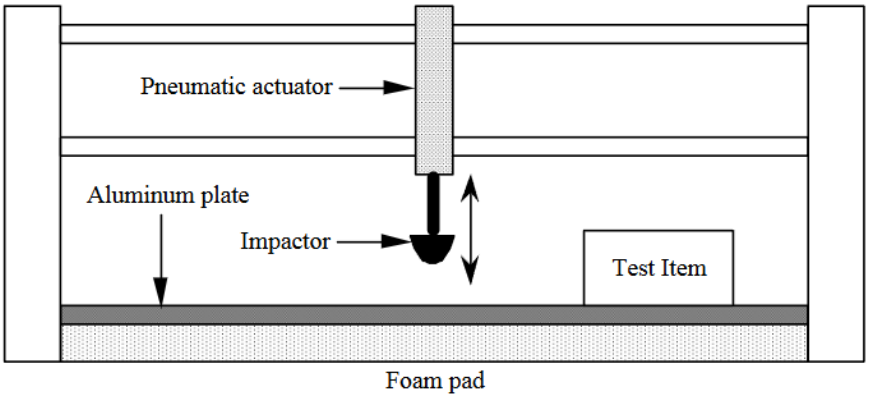

Fig. 1.5 Mechanical Impulse Pyroshock Simulator

Simplified mechanical alternatives using commercially available equipment have been utilized. One such example is the use of nail guns as impulse generators. Although significantly less complex and lower in energy than custom built gas or

pendulum systems, nail guns can still deliver mechanical pulses suitable for shock simulations with excellent repeatability [13, 14].

Another popular testing methodology is the use of electrodynamics shaker that convert the electrical energy in kinetic energy via a voice coil and a magnetic armature. Such method is beneficial since it is possible to generate a variety of signals with great repeatability, giving the most amount of control over the spectrum. However, shakers are limited in the amount of force and acceleration that they can produce, with commercially available models that go up to 2000 g at a frequency of 5 kHz [15].

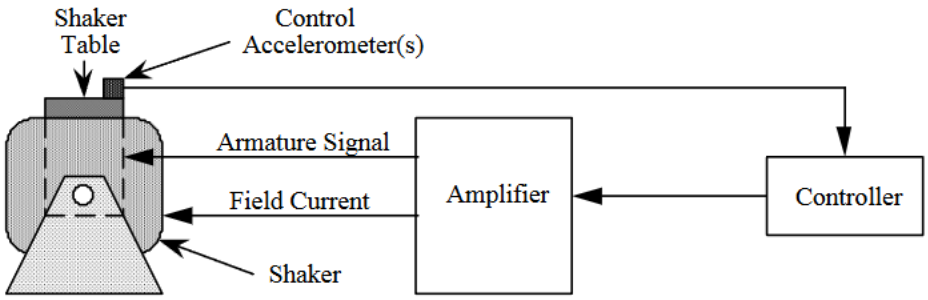

Fig. 1.6 Electrodynamic Shaker exciter

A more recent technique is **laser induced excitation**, where localized surface heating creates thermoelastic stresses that generate high frequency waves in the test fixture. Using this method, Lee et al. [7] achieved peak-to-peak accelerations of 7000 g at 70 kHz, making it a promising high frequency pyroshock simulation method.

1.2 Impact overview

Impact is the phenomenon of at least two bodies colliding with each other, typical characteristics are the short-time frame, the rapid dissipation of energy and high force exchanged. These phenomena can be analyzed in two different ways:

- The so called **discrete method**. this method assumes that the configurations of the bodies remain largely unchanged during the impact. Two distinct moments, before and after the collision, are defined, and the exchange and dissipation of

energy are modeled using coefficients such as the Coefficient Of Restitution (COR) and the impulse ratio [16]. This approach is typically best suited for rigid body impacts.

- The **continuous method**. This approach focuses on the continuous interaction and force exerted during the impact, providing a more realistic representation of the system behavior. It accounts for elastic and/or plastic deformation of the bodies and the resulting energy dissipation.

During impact, deformation leads to energy being dissipated through various mechanisms. A portion of the initial kinetic energy excites vibrations within the bodies via wave propagation. Notably, energy loss is minimal when the colliding bodies have similar sizes, as waves can transfer energy back efficiently [17]. In contrast, significant energy loss occurs when the larger body waves cannot rebound in time to transfer energy to the smaller body. Other dissipation mechanisms include permanent deformation, material damping, and the generation of heat and sound.

The energy loss can be quantified thanks to COR, commonly denoted as e. To respect the conservation of energy, e should always be defined within the range $0 < e \leq 1$ where 1 is perfectly elastic restitution, and 0 is complete energy dissipation. In some cases, in the presence of chemical reactions for instance, the amount of energy after the impact can be greater than pre-impact energy, resulting to e higher than 1. The COR depends on factors such as geometry of the bodies, impacting velocity and materials properties. Several models have been proposed: Newton [18], Poisson [19], Stronge [20], Zener [21] and Weir-Tallon [22] provide frameworks for estimating e.

Despite the complexity of impact dynamics it is possible to define a compression and a restitution phase for every case. The compression phase goes from the time of first contact to the instant where maximum deformation is reached and the velocity of the body is nil; the restitution phase, instead, is the remaining time until the separation. Typically, the two phases are not symmetrical.

The first to quantify this asymmetry was Newton, who defined COR as the ratio of the relative velocity after impact to the relative velocity before impact, along the normal direction. This definition captures the overall energy dissipation during the collision:

$$e = \frac{-u_r}{u_i} \tag{1.9}$$

where u_r is the relative velocity of separation (post-impact) and u_i is the relative velocity of approach (pre-impact).

Subsequently Poisson decided to introduce a COR definition based on the ratio of impulses during the restitution and compression phases. An impulse is the time integral of the force acting on a body over the duration of the impact.

$$e = \frac{P_r}{P_c} \tag{1.10}$$

Where P_r and P_c are the impulses during restitution and compression, respectively.

Both methods lead to inconsistencies when the impact is perfectly elastic, they produce non nil energy losses along the normal direction. Observing the limitations of previous definitions, Stronge proposed a COR based on the work done by normal forces during the compression and restitution phases.

$$e^2 = \frac{W_r}{W_c} \tag{1.11}$$

Where W_r is the work done during the restitution phase, and W_c during the compression phase.
To address the additional energy loss due to wave propagation in cases where the colliding bodies have vastly different dimensions, Stronge further refined his definition:

$$e^2 = \frac{W_r - W_w}{W_c} \tag{1.12}$$

Here, W_w accounts for energy lost due to wave propagation, which is particularly significant when large bodies collide with much smaller ones.

One of the most widely adopted estimates of the COR is given by Zener. He characterized an elastic impact of a sphere with a finite thickness plate, using physical parameters related to geometry and material of impacting bodies.

$$e = exp(-1.719 \cdot \lambda) \tag{1.13}$$

Where λ is the inelasticity factor defined as:

$$\lambda = \frac{1}{4\sqrt{3}} \left(\frac{\pi\rho_s}{\rho_p}\right)^{3/5} \left(\frac{2R_s}{t}\right)^2 \left[\frac{u_i^2 \rho_p (1-\nu_p^2)}{E_p}\right]^{1/10} \left[1 + \frac{E_p(1-\nu_s^2)}{E_s(1-\nu_p^2)}\right]^{-2/5} \tag{1.14}$$

where:
- ρ_s, ρ_s is the density of the sphere and plate material respectively
- R_s is the radius of the sphere
- t is the thickness of the plate
- u_i is the impact velocity
- ν_s, ν_p is the Poisson ratio of the sphere and plate material respectively
- E_s, E_p is the Young modulus of the sphere and plate material respectively

This formulation aligns with real data only in the case of plates thin enough to allow several wave reflections during the contact time so that a significant portion of the energy is converted in flexural energy [23].

On the other hand the model proposed by Weir and Tallon is developed for a body impacting on thick block so the COR is in this case independent of sphere size and plate thickness.

$$e = \left(\frac{3.1}{\rho_s^{1/8} \left(\frac{1-\nu_s^2}{E_s} + \frac{1-\nu_p^2}{E_p} \right)^{-1/2}} \right) \left(\frac{\sigma_y^5}{u_i^2} \right)^{1/8} \tag{1.15}$$

where σ_y is the yield strength of the material.
Due to the founding assumptions of this model it has been found that, contrary to Zener's, the prediction is accurate in case of ratios of $thickness/diameter$ of the sphere closer to one [23].

1.2.1 Continuous Approach

As previously mentioned, discrete methods can lead to violations of the energy conservation principle during impacts with friction. Additionally, these methods often struggle to generalize to complex scenarios, such as impacts involving multiple bodies.

Continuous contact models offer a solution to these issues by expressing the impact force as a function of the local indentation of the bodies. The first continuous model was proposed by Hertz, specifically for elastic contact (unitary coefficient of restitution, $e = 1$), where the relationship between force and deformation is nonlinear. The key assumptions of Hertz's theory are that the deformed area is small relative to

the bodies surfaces and that elastic wave propagation is negligible and no friction is present. The force-indentation relationship is given by:

$$F(\delta) = k\delta^n \tag{1.16}$$

Where k and n are constant depending on material and geometric parameters of the bodies, like Young's modulus E , Poisson's ratio ν and surface curvature. Because this model assumes elastic impacts, it is best suited for scenarios involving low velocities and hard materials. However, both Gugan [24] and Cross [25] demonstrated that most energy losses during an impact occur after the point of maximum compression. Consequently, the compression phase can be effectively modeled using Hertz's theory even in cases where only about 60% of the kinetic energy is retained.

To account for the behavior of plastic deformation under impact forces, Hertz's theory can be modified by introducing the concepts of permanent deformation, $\delta_{permanent}$, as well as the maximum force and indentation achieved during contact. The resulting relationship is expressed as:

$$F(\delta) = F_{max}\left(\frac{\delta - \delta_{permanent}}{\delta_{max} - \delta_{permanent}}\right)^n \tag{1.17}$$

where:
- F_{max} is the maximum force
- δ is the indentation
- $\delta_{permanent}$ is the permanent indentation after unloading
- δ_{max} is the maximum indentation during loading
- n is exponent governing the shape of the unloading curve based on material properties

In subsequent developments, Hunt and Crossley [26] proposed a model to incorporate energy dissipation into the force deformation relationship by introducing nonlinear damping. The force is expressed as:

$$F(\delta) = b\dot{\delta}^n\delta^p + k\delta^n \tag{1.18}$$

It can be noted that damping depends, other than deformation speed, also on indentation. This dependency can be attributed to the fact that the contact surface area

increases with deformation, which leads to greater energy dissipation since more material is involved. Assuming low impact velocities the COR can be expressed as a function of $\dot{\delta}$ and α, which is a parameter related to material, geometry and kinematics of the impacting bodies, as in Eq. 1.19.

$$e = 1 - \alpha\dot{\delta} \tag{1.19}$$

Hunt and Crossley also derived the following relationship between the damping factor b and the contact stiffness k:

$$b = \frac{3(1-e)}{2}\frac{\dot{\delta}}{u_i} \tag{1.20}$$

As shown in [27], substituting equations (1.19) and (1.20) in equation (1.18) it is possible to obtain:

$$F(\delta) = k\delta^n\left[1 + \frac{3(1-e)}{2}\frac{\dot{\delta}}{u_i}\right] \tag{1.21}$$

Other continuous models instead employ trigonometrical functions to descibe the force profile during contact. Hunter [28] proposed a half sine pulse, with period τ:

$$F(t) = F_{max}sin\left(\frac{\pi t}{\tau}\right), \quad t \in [0,\tau] \tag{1.22}$$

where τ is the contact time defined as:

$$\tau = 4.53\left[\frac{4}{3}\rho_s\pi\left(\frac{1-\nu_s^2}{\pi E_s} + \frac{1-\nu_p^2}{\pi E_p}\right)\right]^{2/5} R_s u_i^{-1/5} \tag{1.23}$$

Reed [28] modified the model raising the sine function to the power of $3/2$ and introducing an analytical formulation to estimate the maximum contact force. However, the time estimation remains consistent with equation (1.23). The modified force profile is expressed as:

$$F(t) = F_{max}sin^{3/2}\left(\frac{\pi t}{\tau}\right), \quad t \in [0,\tau] \tag{1.24}$$

where the maximum contact force, F_{max}, can be expressed as:

$$F_{max} = 1.917\rho_s^{3/5}\left(\frac{1-\nu_s^2}{\pi E_s}+\frac{1-\nu_p^2}{\pi E_p}\right)^{-2/5} R_s^2 u_i^{6/5} \tag{1.25}$$

Due to the impossibility of obtaining a perfect conservation of energy (COR = 1) a model has been proposed in [4] that takes into account the partial loss of energy due to inelastic phenomena. This model separates the impact event into two phases: compression and restitution. Each phase is characterized by a distinct time duration, and the force profile is approximated using a von Hann function (also known as a raised cosine function). This approach allows for more accurate modeling of the inelastic phenomena during impact.

To create the force signal in the time domain, the first necessary parameter is the contact time, which can be estimated using Hertz contact theory under the assumption of a spherical, isotropic, and homogeneous body impacting a plate. For these conditions, the impact is elastic, and the contact time is expressed as:

$$\tau = 2.9432 \cdot \left[\frac{15m_s\left(\frac{1-\nu_s^2}{E_s}+\frac{1-\nu_p^2}{E_p}\right)}{16R_s^{1/2}u_i^2}\right]^{\frac{2}{5}} \tag{1.26}$$

where m_s is the mass, R_s the radius and u_i the velocity of the impacting sphere. Contact time is then divided to describe the compression and restitution phase: as previously mentioned the first one is completely elastic so its duration can be half of the perfectly elastic impact $\tau_{el} = \tau/2$.

In the second phase, permanent deformation makes the duration a function of the coefficient of restitution e, so Zener's model (1.14) is used to correct the duration as $\tau_{an} = e\tau_{el}$.

The second parameter is the maximum force exchanged during contact computed using the momentum of the impacting body

$$F_{max} = \frac{m_s u_i}{\int_0^{\tau_{el}} \frac{1}{2}\left[1-cos\left(\pi\frac{t}{\tau_{el}}\right)\right]dt} \tag{1.27}$$

To account for the effects of energy dissipation, the final force curve is modeled as asymmetric.The force profile $F(t)$ is defined as:

$$F(t) = \begin{cases} \frac{F_{max}}{2}\left[1 - cos\left(\pi \frac{t}{\tau_{el}}\right)\right], & t \in [0, \tau_{el}] \\ \frac{F_{max}}{2}\left[1 - cos\left(\pi \frac{t-\tau_{el}(1-e)}{\tau_{el}}\right)\right], & t \in (\tau_{el}, \tau_{el} + \tau_{an}] \end{cases} \tag{1.28}$$

In Figure 1.7 three different force profiles normalized in amplitude and duration are shown to underline the different shapes produced by the Hunter, Reed and the asymmetric pulse based on the von Hann curve.

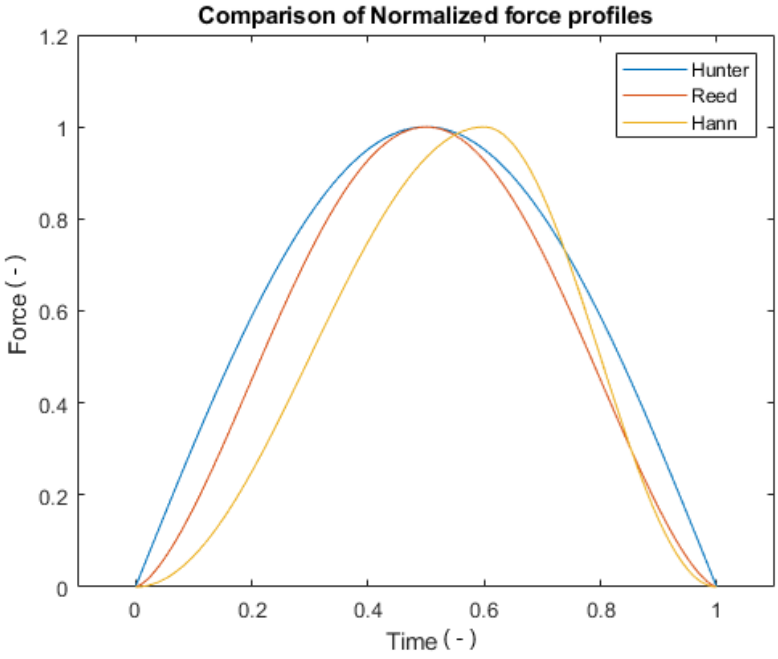

Fig. 1.7 Force profile obtained by Hunter, Reed and asymmetric von Hann Models. Obtained with a COR of 2/3

1.2.2 Data-Driven Models

Over the past decade, continuous progress in Machine Learning (ML) algorithms has significantly broadened their application in the modeling of complex physical systems. One of the applications that can benefit is contact mechanics, where tradi-

tional analytical or numerical approaches can struggle to describe the phenomenon, especially when large amounts of energy is dissipated.

A notable example of this application can be found in the use of learning models to characterize the mechanical behavior of additively manufactured structures. In these studies, the compressive deformation of complex geometries during impact with a reference aluminum plate was successfully modeled using deep neural networks, enabling a data-driven understanding of material response [29].

Similarly, ML methods have been applied to the domain of armor design, where predicting projectile behavior post-impact is critical for both defense and safety applications. Neural networks have been trained to estimate the residual velocity of projectiles after penetration of both single layer and multi layer armor systems [30]. In addition to predictive tasks, ML has been utilized to generate synthetic yet statistically meaningful datasets for high rate dynamic events, such as vehicular collisions, blast mitigation scenarios, and shock propagation through electronic components [31]. These synthetic datasets are especially valuable in scenarios where physical experimentation is expensive, dangerous, or infeasible.

The utility of machine learning extends beyond impact force prediction to post impact characterization. For example, models have been developed and validated to describe damage accumulation in fiber reinforced polymer composites subjected to compressive impacts [32]. Additionally, ML based frameworks have been applied to track material degradation and deformation under repeated impact loading [33].In robotics, ML has been integrated with physics based models to improve the accuracy of predictions in real world contact scenarios. A notable example is the hybrid approach presented in [34], where 12 separate models (one for each degree of freedom of the impacting bodies) were trained and validated using a synthetic dataset simulating a ball bouncing on a flat surface.

Building on the promising outcomes of these studies, this thesis focuses on developing ML models trained on experimentally acquired data to predict contact forces during impact events.

1.3 Objectives

Despite considerable advances in both analytical and data-driven approaches for modeling contact mechanics during impact events, the literature presents significant gaps. Most classical analytical models, including those by Hunter, Reed, and Zener, assume idealized conditions and often neglect critical factors such as complex geometries, material heterogeneity, and dynamic dissipative phenomena. Consequently, they can fail to capture the non-linear behaviors observed in real experimental setups, particularly in aerospace structures where transient mechanical loads like pyroshocks are prevalent.

Furthermore, while recent studies have demonstrated the potential of machine learning frameworks to predict contact forces and damage accumulation, these models often rely on synthetic, highly simplified test conditions. Those that are based on experimental data are focused on material characterization through impacts and not force characterization. The lack of validation against real experimental data, especially in scenarios involving high frequency, high amplitude shocks, limits their generalizability and practical application.

To address these gaps, this thesis is structured around the following objectives:

- **Development of a Data-Driven Contact Force Model**
  Assess the feasibility of modeling contact forces in the time domain using a ML approach. The model will be trained and validated on an experimental dataset generated through controlled hammer impacts. Its performance will be compared with classical analytical contact models from the literature, highlighting potential benefits in terms of generalizability, accuracy, and the ability to capture non-linear behaviors.

- **Design and Implementation of the Experimental Setup**
  Finalize the test bench at Politecnico di Torino, consisting of a compressed air gun and a plate resonator, and design a robust measurement chain capable of capturing transient mechanical phenomena with high fidelity. This includes precise measurement of impact velocity, chamber pressure, and contact force to ensure that the acquired data is of sufficient quality for model training and validation.

- **Validation of the Velocity Prediction Model**
  Use the test data to validate a velocity prediction model capable of reliably estimating projectile speed based on input parameters. This reduces the need for extensive calibration and forms a critical component of the digital twin of the test system.

Through these objectives, this thesis aims to contribute to the development models for predicting contact forces in complex impact scenarios. These models can be integrated into digital twin frameworks reducing the resources required for experimental campaigns, and enhancing the understanding of systems subjected to pyroshocks.

Chapter 2

Experimental Setup

The experimental test bench consists in a resonant plate suspended by a frame. The plate is excited using a compressed air cannon that propels projectiles toward the plate. In this chapter each component is briefly described and a design for a safety plate is presented alongside with the measurement chain and a numerical model for the exit velocity of the bullet.

2.1 Components

2.1.1 Frame and resonant plate

The resonant plate frame is structure which primary task is to suspend the plate by using chains connected to the horizontal upper member to simulate free-free conditions, as shown in Figure 2.1. The design is focused on maximizing the size of the plate that can be suspended in the given dimensions constraint of the laboratory space, in particular plates made of steel of up to 2000 x 1000 x 50 mm weighing around 800 kg can be used as resonators. The structure is constructed entirely of standard structural steel bars (S355) and is bolted to the ground using chemical anchors and M20 screws, mechanical isolation from the floor is achieved using rubber mats approximately 6 mm in thickness. In this configuration the structure can withstand impacts of masses of $m = 1\ kg$ traveling at speed up to $v = 80\ m/s$. A detailed description and a structural analysis of this frame are presented in [35].

The motion of the plate after impact is restricted using one additional connections between the plate and the lower section of the steel frame, namely using elastic ropes. This is particularly important in case of light plates that, due to their lower inertia, may oscillated with large angular displacements.

Chains are used to suspend the plate, as they offer both support and a simple means of adjusting its vertical position. By selecting different chain links to attach the suspended mass, the height of the plate from the floor can be easily modified in discrete increments of 56 mm, the chain pitch. This setup allows for controlled variation of the impact position relative to the plate edge, enabling investigation into how proximity to the boundary influences the contact response.

Fig. 2.1 Suspension frame and resonant plate

The plate is made out of steel in a diamond-like shape and has a total thickness of 10 mm. It is fixed to the upper member through two attachment points and it has a single connection to the lower member as seen in Figure 2.1, meanwhile, in Figure 2.2 the CAD model with the exact dimensions is reported.

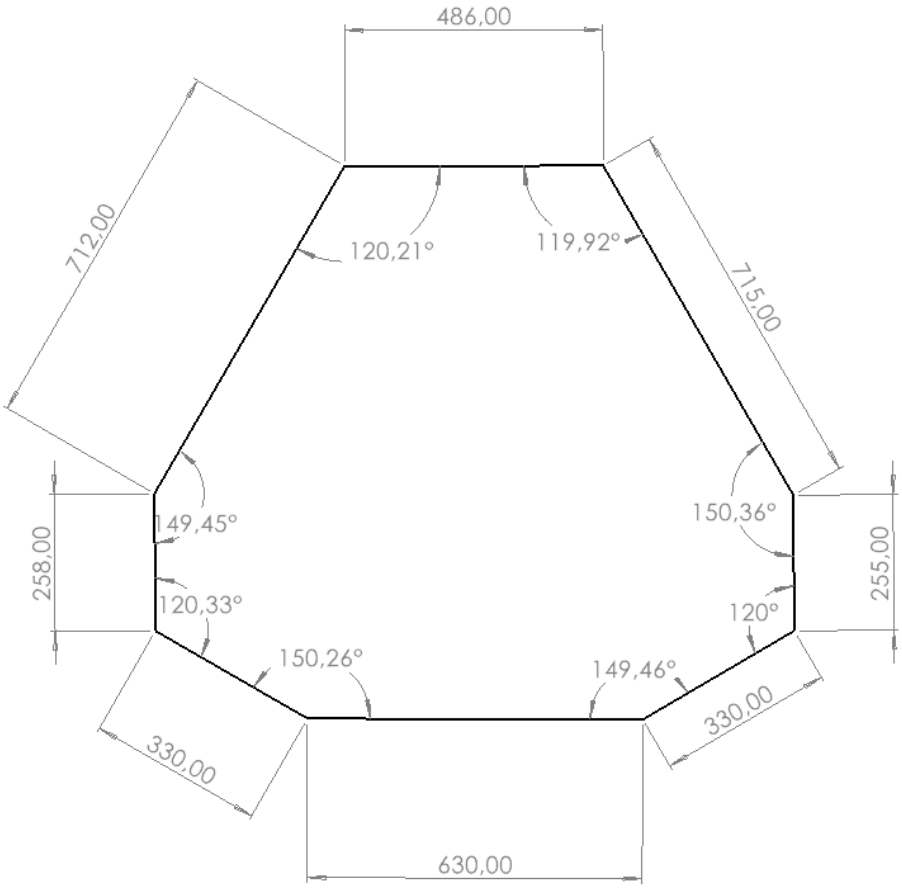

Fig. 2.2 Dimensions of the resonant plate

All critical connections, those that allow suspension of the testing plate are designed to have a Safety Factor (SF) higher than 3.9, while the ropes used to limit the angular displacement have SF = 2.3 since in case of failure the consequences are far less severe. The operational loads considered in Table 2.1 are taken from a previous work [4] that considered the most crucial impact with momentum of 80 kgm/s and two different plates: a steel one that generates the maximum load on the chain suspending the plate and a light aluminum plate that, due to large oscillations after impact, generates the highest load on the constraining ropes.

Table 2.1 Components used to suspend the plate and relative safety factor

Component	Load in operation (N)	Maximum Rated Load (N)	SF
Chain	7765	80000	10.3
Shackle	7765	31882	4.10
Connecting Links	7765	30901	3.98
Rope	7550	34825	2.3

2.1.2 Pneumatic Gun

The objective of this component is to accelerate the impacting object to the desired speed in order to excite the plate in the most correct manner. This type of exciter has been deemed the most appropriate, since it increase the repeatability of the impulse, reduces the possibility of secondary impacts. The gun is composed of two main parts, as seen in Figure 2.3: a barrel and a gas chamber. The chamber is a tank of volume $V = 9.5\ l$ certified for pressures up to $P_{max} = 2\ MPa$. The barrel is a steel tube of internal diameter $\phi = 49\ mm$ and a length of 1560 mm.

The two components are connected by a 50 mm pneumatic ball valve (Effebi dga083ax00) with an actuation pressure of 0.8 MPa, capable of sealing gasses up to 6.48 MPa . The valve is controlled electronically allowing to set opening times from 0.1 s to 30 s, the controller allows to select a reloading mode that prevents the valve from opening during reloading procedures for increased safety.

The gun is mounted on a frame using C-shaped clamps. The structure can be easily moved on casters to control the horizontal impact position and, after regulation, is it lifted by rubber supports that also allow leveling using threaded rods. The gun is positioned next to the resonant plate, leaving enough clearance to avoid contact during oscillation but not enough to allow the projectile to exit the barrel. This ensure an higher degree of safety for the operators. Furthermore, during any activity that require the operator to be in the trajectory of the bullet tw0 12 mm pins will be inserted in the radial holes along the barrel. The same holes, during testing, reduce the chance of secondary impacts. Once the projectile hits the plate the pneumatic valve will be closed, the holes allow residual air to exit the barrel without increasing pressure. If not for this the air downstream of the bullet would behave as a stiffness in SDOF m-k system.

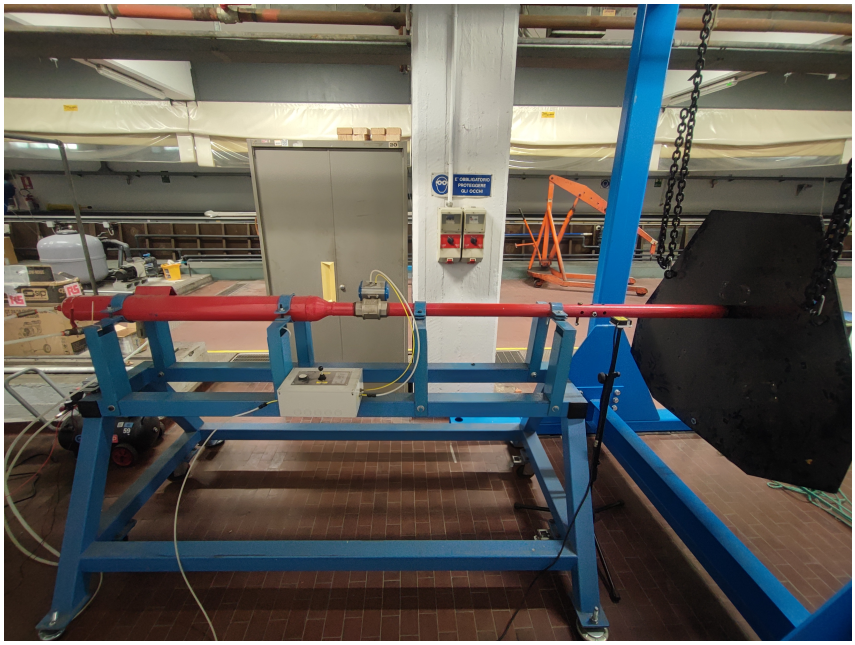

Fig. 2.3 Pneumatic gun

The compressed air is generated by a portable compressor, with maximum operating pressure of 10 MPa and 24 liters in capacity. The pneumatic circuit of the test bench is composed as follows: the compressor is connected to a pressurized line with two branches, the first one feeds the pneumatic ball valve. The second branch is connected to a pressure regulator used to control the feeding pressure of the air tank. After the regulator a manual two position ball valve is placed to isolate the tank from the compressor. The pressure in the tank is monitored with a digital pressure transducer (GENSPEC GS 4002) with built in electronic conditioning. In this way the air compressor can be set up to deliver 8 bar of pressure, the actuation pressure of the valve, and the regulator allows to tune the tank pressure in the range 0 - 8 bar In Figure 2.4 a visual representation of the circuit is shown.

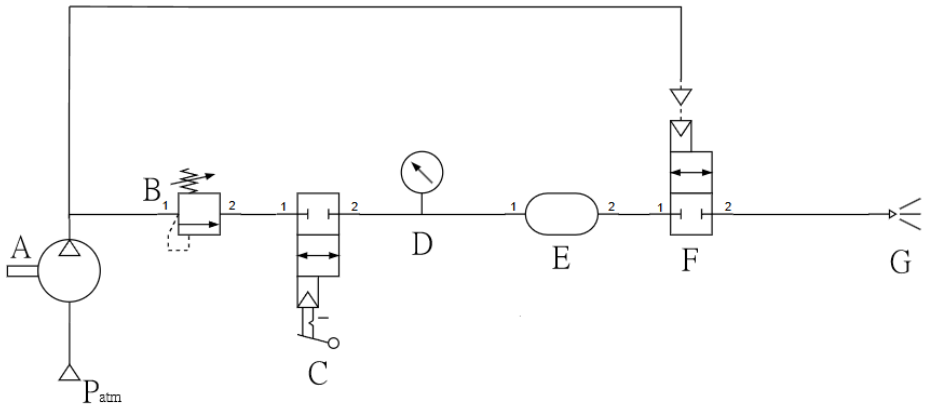

Fig. 2.4 Pneumatic Circuit of the pneumatic gun, A: compressor, B: pressure regulator, C: manual ball valve, D: digital and analog manometer, E: tank, F: pneumatic ball valve, G: barrel

The projectiles used with this pneumatic gun are composed of two modular components: a main body and an interchangeable front plate. The main body is a cylindrical element with a fixed diameter of 48 mm, (Figure 2.5b) designed to allow variation in the overall mass of the projectile by adjusting its length. This enables to control over the momentum of the impacting body.

On one end of the main body, two threaded M6 holes are machined to enable secure attachment of the front plate. The front component of the projectile, shown in Figure 2.5a, is a replaceable cylindrical plate, also featuring two countersunk M6 holes aligned with those on the main body. This modular design serves two main purposes: it allows for quick and easy replacement of the impact surface, the part most susceptible to damage, and facilitates flexibility in tuning the impact characteristics by changing the curvature or material of the front plate. By decoupling the main body from the impact head, this system significantly reduces the manufacturing and maintenance costs associated with projectile damage or variation.

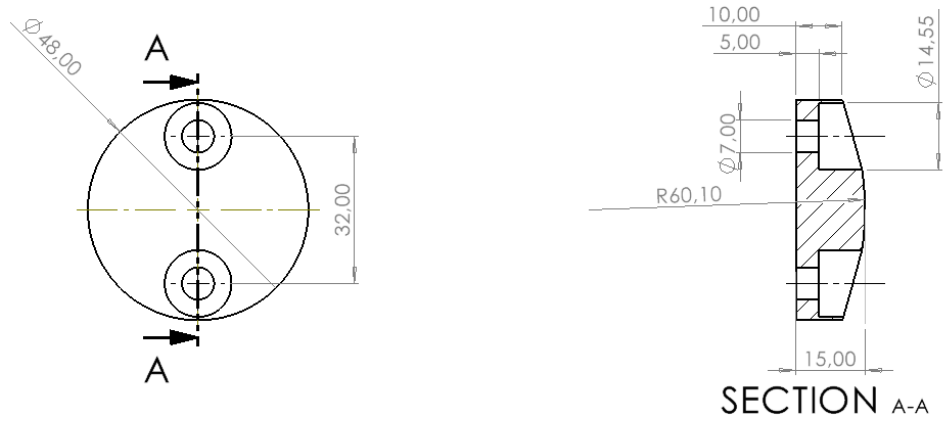

(a)

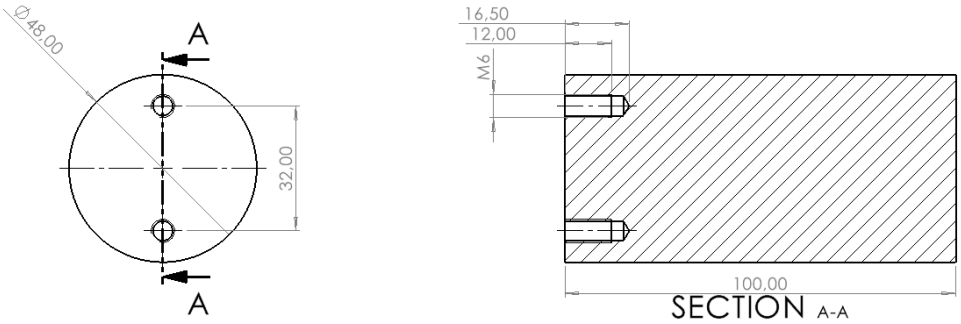

(b)

Fig. 2.5 Modular bullet design: (a) interchangeable bullet tips; (b) bullet main body

2.1.3 Safety plate

Due to the potential catastrophic damages in case of the resonant plate failure a secondary plate is designed to stop the projectile from exiting the laboratory space. The design is carried out using the concept of ballistic limit velocity, u_{bl}, which is the velocity at which projectiles have a 50% probability of penetrating a finite thickness plate of metal [36]. The model used for calculation depends on the material of the plate itself. Since the compressed air gun is designed to propels projectiles up to 1 kg at 80 m/s to guarantee a safety margin all plates are verified to withstand projectiles of 1 kg traveling at 150 m/s.

Assuming an sluminum construction, Nishiwaki [37] proposed and validated an analytical model to predict ballistic limit velocity:

$$u_{bl} = \left(\frac{gP_0}{\rho_p} \left[\exp\left(\frac{\rho_p}{2m_s} \pi d^2 h \right) - 1 \right] \right)^{1/2} \tag{2.1}$$

where:
- ρ_p is the density of the target plate
- h is theplate thickness
- g is the acceleration due to gravity
- m_s is the projectile mass (assumed constant)
- d is the projectile diameter
- P_0 is the experimental coefficient for aluminum

Using a diameter of 48 mm, close to the inner diameter of the barrel, to achieve a ballistic limit velocity of 150 m/s a plate thickness of around 10 mm is required.

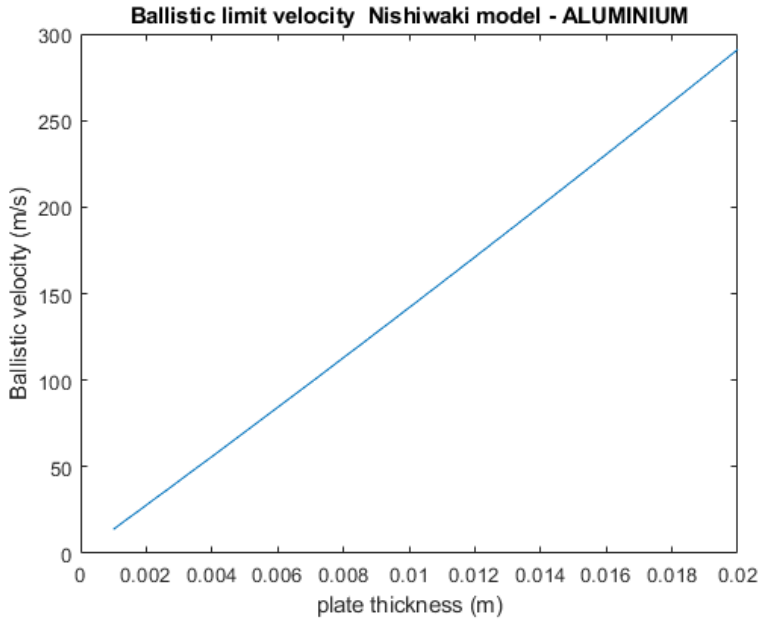

Fig. 2.6 Ballistic limit velocity for a 1 kg aluminum projectile (d=48 mm) impacting an aluminum plate.

Instead, if a steel plate (S355 just like the plate frame) is used, the most conservative model is the one proposed by Forrestal [36] :

$$u_{\text{bl}} = \left(\frac{\pi d^2 h \sigma_s}{2 m_s} \right)^{1/2} \tag{2.2}$$

Where σ_s is the stress required to open a cyindrical hole in plate based on the work of Bishop [38]:

$$\sigma_s = \frac{\sigma_y}{2} \left(1 + \ln \left[\frac{6(1-\nu)K}{(5-4\nu)\sigma_y} \right] \right) \tag{2.3}$$

where:
- K is the bulk modulus of the plate
- σ_y is the yielding strength
- ν is the Poisson's ratio

To achieve a ballistic limit velocity with a projectile of 48 mm a steel plate of around 5 mm is necessary.

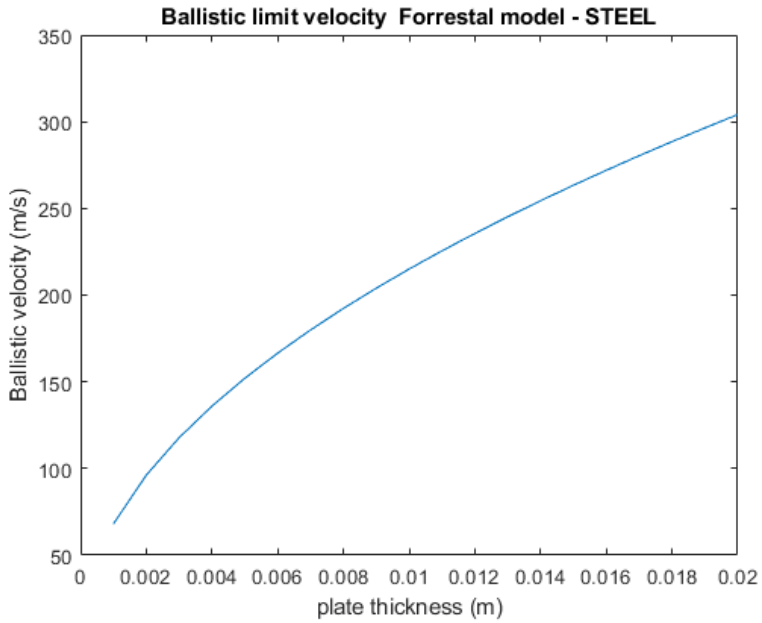

Fig. 2.7 Ballistic limit velocity for a 1 kg aluminum projectile (d=48 mm) impacting a steel plate.

2.2 Sensors and acquisition

In this section all the sensors constituting the measurement chain are described along-side with the acquisition system. An overview of the entire chain is presented in Figure 2.8.

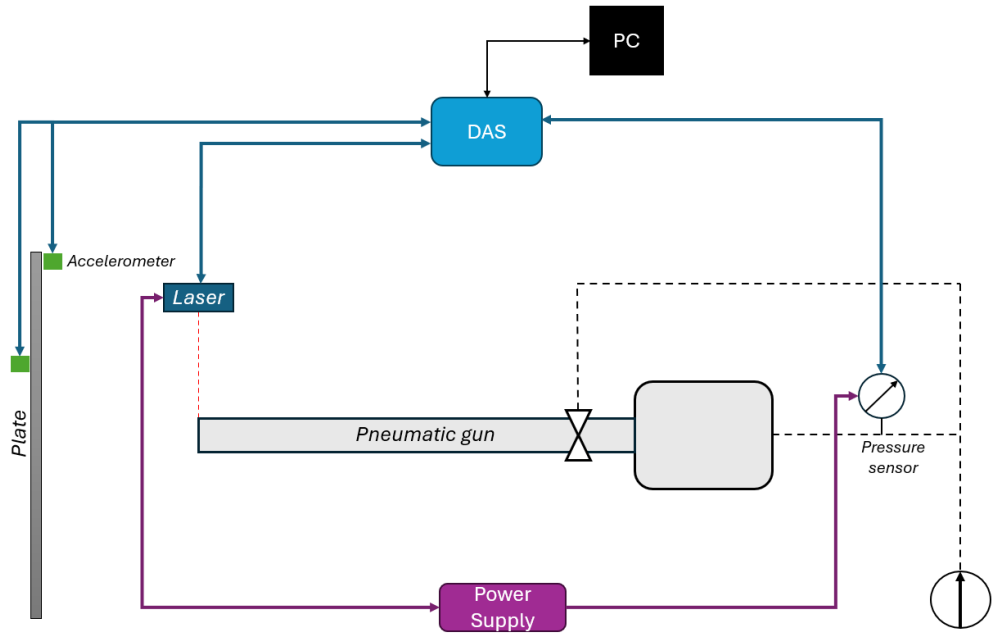

Fig. 2.8 Measurement chain

2.2.1 Sensors

To measure the **exit velocity** of the bullet, a laser displacement sensor (Panasonic LM10 ANR1215) is employed. The sensor is capable of measuring distances ranging from 180 mm to 80 mm from its face, with a resolution of 20 μm. It is mounted on a tripod and positioned so that its beam is directed radially through a small aperture in the barrel, targeting the inner wall. As the bullet passes through the laser beam, the measured distance decreases by the bullet diameter. By identifying the time instants at which the displacement measurement changes and knowing the bullet length, the bullet velocity can be accurately calculated.

The **pressure** evolution in the chamber upstream of the valve is measured using a pressure sensor, GENSPEC GS 4002, capable of reading in the range 0 - 16 bar,

threaded just before the inlet of the chamber. The sensor is calibrated by using a reference trusted manometer across three load-unload cycles form 0 bar to 4 bar in steps of 1 bar, to these points a first order polynomial has been fitted. The obtained sensitivity is 0.5621 V/bar with an offset of 0.3624 V.

To measure the **response of the plate**, two PCB Model 350B43 triaxial accelerometers are employed. These sensors have a measurement range of $\pm 10000\,g$, a nominal sensitivity of approximately $0.5\,\mathrm{mV/g}$, and a mass of approximately 27 g each. The positioning of the accelerometers is chosen to capture the dynamic response of the plate accurately.

The peak **contact force** was estimated from the projectile momentum, assuming complete transfer of momentum during impact to the plate:

$$m_s u_i = \int_0^\tau F(t)dt \tag{2.4}$$

Using a raised sine function $F(t) = F_{max} sin^2(\frac{\pi t}{T})$ the maximum force can be expressed as follows:

$$F_{max} = \frac{2m_s u_i}{T} = \frac{2m_s u_i}{\tau} \tag{2.5}$$

Considering the maximum desired speed of 80 m/s a mass of 1 kg and a contact time of $1 \cdot 10^{-4}$ s :

$$F_{max} = \frac{2 \cdot 80 \cdot 1}{1 \cdot 10^{-4}} = 1600\ kN \tag{2.6}$$

This estimate is further supported by the machine learning model presented in Chapter 4, which predicts a peak force of 1520 kN.

These forces can be measured indirectly with accelerometers using a similar methodology to that described in Chapter 4 Eq. 4.2.

To start an instrumented hammer is used to excite the plate in the point where the bullet will collide, the response of the plate will be register by one of the accelerometers. Using the `tfestimate` in MATLAB it is possible to find the transfer function between acceleration and force:

$$\mathrm{tf}(\Omega) = \frac{a(\Omega)}{F(\Omega)} \tag{2.7}$$

Using the transfer function it is possible to filter out the dynamic behavior of the plate and find the acceleration as if the sensor was exactly co-located with the load

cell. The plate dynamic behavior will be the same even when the excitation is given by the bullet so using the same tf it is possible to correct the acceleration signal as if the accelerometer was positioned exactly at the impact location:

$$a_{corrected}(\Omega) = \frac{a(\Omega)}{\mathrm{tf}(\Omega)} \tag{2.8}$$

After this, using Newton's laws of motion the force can be computed:

$$F(t) = -m_p \cdot \mathrm{ifft}\left(a_{corrected}(\Omega)\right) \tag{2.9}$$

where:
- m_p is the mass of the plate
- ifft is the Inverse Fast Fourier Transform

Indirectly computing force does not introduce significant error on the measurement. Performing the aforementioned procedure on a hammer generated database, described in details in [39], the error is very small so the measured and computed force signal are very similar as can be seen in Figure 2.9.

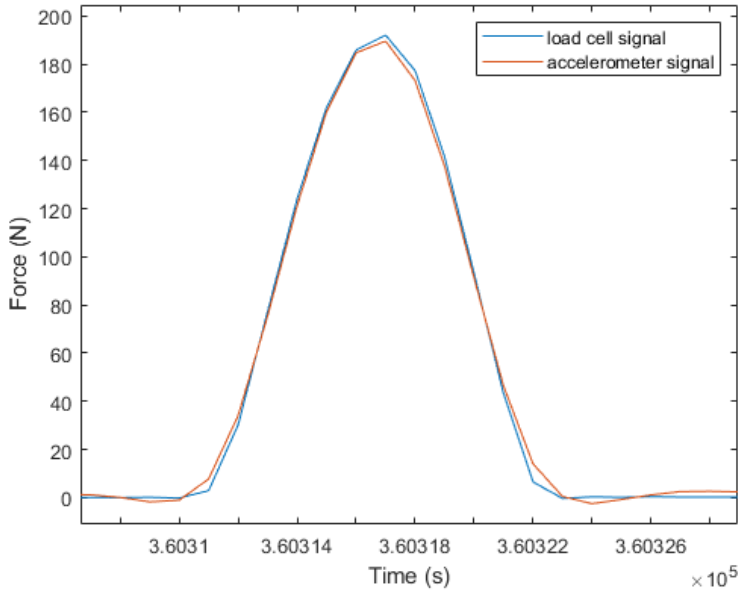

Fig. 2.9 Comparison between force measured by a load cell and computed though acceleration

As an alternative, instead of using the indirect measurement of force obtained from the accelerometer signals, a load cell array could be used: this approach both distributes the load and captures the reaction force over an area rather than a single point.

Although commercial force sensors with capacities exceeding 1000 kN exist, a viable solution is based on the use of the Kistler 9107C piezoelectric force sensors [40], which have a nominal measuring range of 700 kN and a sensitivity of $-4.4\ pC/N$. These sensors are particularly suitable due to their compact form factor and ease of integration: by connecting multiple sensors in parallel, the output charge becomes directly proportional to the total force applied to the array.

In the configuration considered here, four sensors are arranged in a square pattern, with the screw heads positioned on the face opposite to the impact plane. This design ensures a large and uniform measuring surface (see Figure 2.10), enabling a combined measurement capacity of up to 2800 kN . To ensure linearity and improve dynamic response, 20% of the full scale load is reserved for pre-loading the sensors. This leaves an effective operational range of 2240 kN.

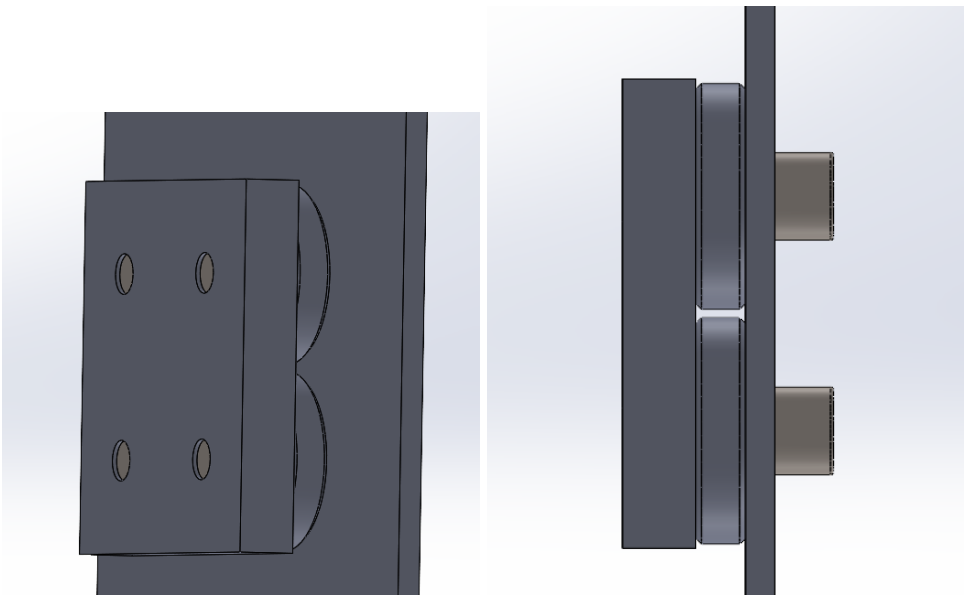

(a) (b)

Fig. 2.10 Load cell array (a) Side view, from left to right: plate on which the impact take place, load cells, resonant plate (b)

To apply the required pre-load, four bolted connections are used. The sizing of these bolts is carried out in accordance with the provisions of Eurocode 3 [41], specifically the tensile resistance criterion:

$$F_{t,E} \leq F_{t,R} = \frac{k_2 f_{ub} A_s}{\gamma_{M,2}} \tag{2.10}$$

where:
- $F_{t,E}$ is the applied tensile force during service,
- $F_{t,R}$ is the design tensile resistance of the bolt,
- f_{ub} is the ultimate tensile strength of the bolt material,
- A_s is the tensile stress area of the bolt,
- $\gamma_{M,2}$ is the partial safety factor for resistance of bolts under tension,
- k_2 is a factor accounting for countersunk or in plane mounting.

For M20 bolts of strength class 10.9, the ultimate tensile strength is $f_{ub} = 1000\,\text{MPa}$, and the tensile stress area is $A_s = 245\,\text{mm}^2$. Assuming a safety factor $\gamma_{M,2} = 1.25$ and $k_2 = 0.9$ (screws directly on the component), the resulting design tensile resistance per bolt is: 176.4 kN. This is more than sufficient for the required pre-load of 140 kN per screw. To complete the threaded connection design, the tightening torque required to achieve the specified pre-load can be estimated using the guidelines from VDI 2230 [42]:

$$T = F_{preload} \cdot \left[0.16S \cdot 0.58 d_2 \mu_g + \frac{D_{km}}{2} \mu g \right] \tag{2.11}$$

where:
- S is the pitch of the screw
- d_2 is the pitch diameter
- μ_g is the coefficient of friction between the screw threads and head and bearing surfaces
- D_{km} is the effective diameter under the bolt head or nut where frictional forces are transmitted.

Assuming a typical friction coefficient of $\mu_g = 0.08$ and using standard geometric values for M20 bolts, the tightening torque required to achieve the desired pre-load is approximately:

$$T \; = \; 320\,Nm \tag{2.12}$$

2.2.2 Acquisition

At most, using load cells, a total of 12 acquisition channels are required to acquire all sensors: six for the accelerometers, and one each for the pressure sensor, the laser, and the four load cells. The sampling frequency is selected based on the expected contact duration and the dynamic response of the plate. Given contact times on the order 10^{-4} s, a minimum sampling rate of 100 kHz is necessary to ensure at least 10 data points during the contact event, allowing for sufficient temporal resolution of the contact force. Furthermore, this sampling rate enables accurate capture of frequency components up to 39 kHz, in accordance with the Nyquist theorem, ensuring that the dynamic response of the plate is faithfully recorded without aliasing.
To maintain consistency across trials, a trigger logic can be implemented to initiate data acquisition upon the pressure drop in the pneumatic circuit feeding the valve opening mechanism.

2.3 Impacting velocity prediction

To achieve a comprehensive digital twin of the test apparatus, it is necessary to develop a mathematical model capable of predicting the muzzle velocity of the projectile at the exit of the barrel. Accurately modeling the projectile velocity can significantly reduce both the calibration time and associated costs during experimental campaigns. An accurate estimate of the impact speed, this model minimizes the number of physical tests required to fine tune the spectral content of the impact, potentially eliminating the need for iterative trial and error adjustments.

The compressed air gun is idealized as a system consisting of a finite volume pressure chamber of volume V_0, connected to a straight cylindrical barrel of length L and diameter d. The projectile, having mass m_s, is initially at rest within the barrel. Upon the release of compressed air at an initial pressure Q_0, the projectile is accelerated along the barrel due to the expansion of the pressurized gas. As the bullet moves forward, the gas volume increases. A schematic of the model is shown in Figure 2.11.

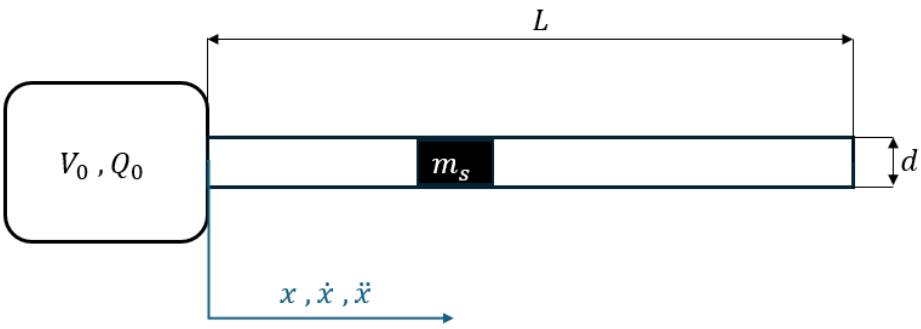

Fig. 2.11 Scheme of the pneumatic gun model

During its motion, the projectile experiences a frictional force resulting from contact between its outer surface and the inner wall of the barrel. This resistive force can be modeled as:

$$f = -\mu_d m_s g \tag{2.13}$$

where:
- μ_d is the coefficient of dynamic friction between the two materials.
- g is the gravitational constant.

Considering relative pressures, the projectile motion is governed by Newton's second law:

$$m_s \frac{d^2x(t)}{dt^2} = Q(t) \cdot A - \mu m_s g \tag{2.14}$$

where:
- $A = \pi d_s^2/4$ is the cross sectional area of the projectile on which the pressure acts.
- $x(t)$ is the projectile position over time.

The expansion of the gas is limited only by the inertia of the bullet and friction, for this reason it will take a very short time: this will prevent heat exchange to the surrounding environment and the evolution is therefore considered adiabatic [43]. Assuming air behaving as a perfect gas, the pressure can be expressed as a function of displacement:

$$Q(t) = \frac{Q_0 V_0^\gamma}{V(x)^\gamma} = \frac{Q_0 V_0^\gamma}{[V_0 + A \cdot x(t)]^\gamma} \tag{2.15}$$

where:
- $\gamma = 7/5$ is the heat capacity ratio of a perfect diatomic gas.

Combining the pressure evolution equation (2.15) with the equation of motion (2.14) leads to the following second order Ordinary Differential Equation (ODE):

$$\frac{d^2x(t)}{dt^2} = \frac{Q_0 V_0^{\gamma}}{[V_0 + A \cdot x(t)]^{\gamma}} \cdot \frac{A}{m_s} - \mu g \tag{2.16}$$

To solve this ODE numerically, it is first rewritten as a system of two first order ODEs by introducing the velocity $u_s = \frac{dx}{dt}$ and the acceleration $a_s = \frac{du_s}{dt}$.

$$\begin{cases} u_s = \frac{dx}{dt} \\ a_s = \frac{Q_0 V_0^{\gamma}}{[V_0 + A \cdot x(t)]^{\gamma}} \cdot \frac{A}{m_s} - \mu g \end{cases} \tag{2.17}$$

This system is integrated using MATLAB's `ODE45` solver, with initial conditions:

$$\begin{cases} x(0) = 0\ m & \textit{Initial Position} \\ u_s(0) = 0\ m/s & \textit{Initial Velocity} \end{cases}$$

The numerical integration of motion is terminated as soon as the projectile exits the barrel using the `Events` option in the MATLAB ODE solver. To accurately capture the dynamics of the launch process, especially in cases where the initial pressure Q_0 is high and the launch duration is consequently very short, a fixed time step of 0.1 ms is employed. This fine temporal resolution ensures that rapid variations in acceleration, and velocity are adequately resolved.

An important aspect of the modeling is the presence of vent holes along the barrel. In this setup, six large holes are positioned on the barrel wall at a distance of $x = 0.885\ m$ from the valve. These holes allow the expanding gas to vent into the atmosphere once the projectile passes this threshold, effectively ceasing further acceleration. Consequently, the relevant portion of the barrel is limited to the first 90 cm. The muzzle velocity is therefore defined as the projectile velocity at $u_s(t)|_{x=0.885\ m}$, and this value is used for further analyses and validation with experimental data.

This simplified model does not account for some losses, namely:

- Blow-by losses due to air moving through the gap existing between the inner walls of the barrel and the projectile.
- Concentrated pressure drop due to valve.
- Distributed losses in the barrel.
- Aerodynamic drag of the bullet moving through air.

For these reason, other studies introduce a corrective term η reduce the predicted speed. Starting with the same correction presented in [44] $u_s(t)$ becomes:

$$\eta \cdot u_s(t)|_{x=0.885\ m} = 0.5 \cdot u_s(t)|_{x=0.885\ m} \tag{2.18}$$

The velocity variation for different masses and pressure is reported in Figure 2.12

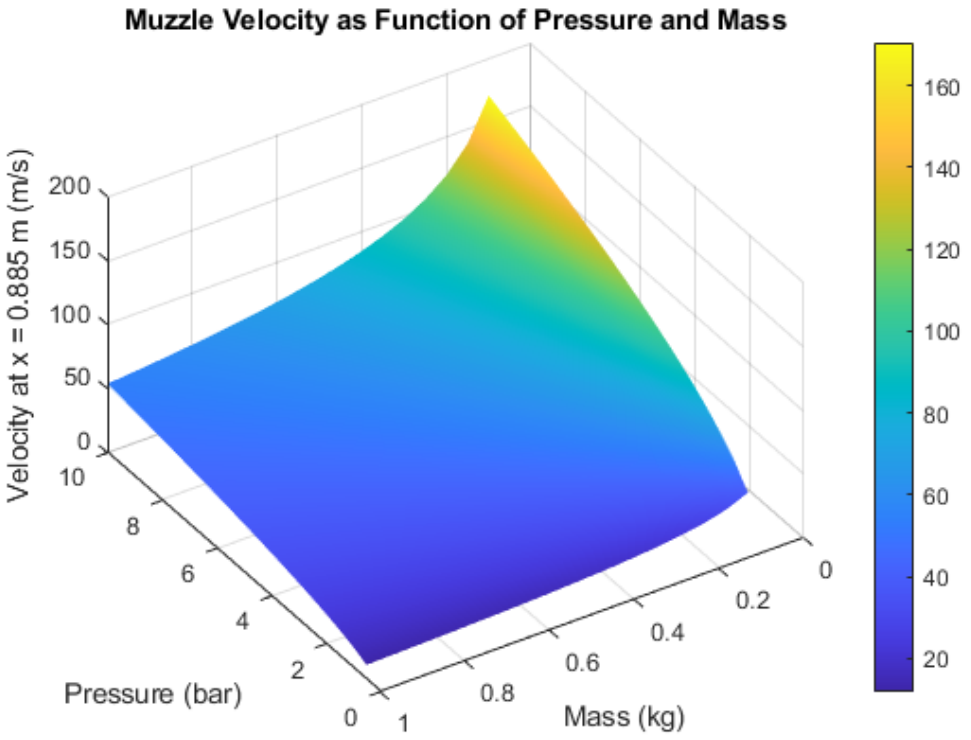

Fig. 2.12 Mass and pressure influence on exit velocity

Chapter 3

Preliminary tests and Design of Experiments

The main objective of this chapter is to define a testing strategy that enables the investigation of how different input parameters influence three main output quantities: the projectile exit speed, the contact force during impact and the duration of contact. At the same time, this Design Of Experiments (DOE) will support the creation of a structured database of pneumatic gun impact events, capturing the effects of input not present in the database described in Chapter 4: bullet mass and plate mass. In the following sections the first few tests performed to asses the proper functioning of the test bench are presented, followed by a comprehensive DOE outlined for future use.

3.1 Preliminary tests

To ensure that components of the pneumatic circuit and the measurement chain are correctly installed few tests are performed with at low pressures and using a 3D printed Polylactic Acid (PLA) bullet to reduce at a minimum the risks connected to the kinetic energy of the bullet. The total mass of the body of the bullet, the two M6 screws and the bullet tip is $m_s = 142.8\ g$ and the length is $L = 85\ mm$. During these test the pressure evolution in the tank and the speed of the bullet are acquired in order to provide a first validation of the bullet velocity numerical model. In Table 3.1 the tank pressure and the relative speeds are presented:

Table 3.1 Tank pressure and measured exit velocity for five low pressure tests

Test #	Pressure (bar)	Speed (m/s)
1	0.2319	10.366
2	0.2651	11.872
3	0.6158	18.973
4	0.4042	13.799
5	0.5784	16.346

3.2 Complete Design of Experiments

DOE is a systematic methodology used to plan and execute tests in a way that efficiently explores how various input parameters influence system outputs. In this context, controllable variables refer to parameters that can be deliberately adjusted during experimentation such as material type, geometry, or air pressure. Each variable is tested at multiple levels, which are specific values selected to span a relevant range for example low, medium, and high pressure. DOE enables not only the evaluation of individual variable effects but also the detection of interactions between them.

To achieve a complete understanding of variable effects and their interactions, a full factorial design is proposed. This method evaluates all possible combinations of the selected variable levels, offering a thorough analysis that outperforms traditional One Variable At a Time (OVAT) approaches. OVAT fails to reveal interactions between variables, whereas the factorial approach ensures a more efficient and insightful exploration of the design space with a lower number of tests.

The controllable variables selected for the tests are: bullet mass, bullet material, tip radius, plate material, plate mass, anvil plate material, presence of an insulating layer, and air tank pressure. Each of these eight factors is assessed at three levels to account for potential non linearities in the system, in accordance with standard DOE practices [45]. Table 3.2 provides an overview of the factors and their respective levels. To investigate the dynamics of impact and the resulting contact forces, a DOE was created involving several physical parameters relevant to the projectile and target. Each factor was chosen based on its potential influence on the amplitude, duration, and frequency content of the contact force signal.

Table 3.2 Controllable variables and their levels for the DOE

Factor Name	**Low Level**	**Medium Level**	**High Level**
Bullet mass (kg)	0.2	0.5	1
Bullet tip	PLA	aluminum	steel
Bullet tip radius (mm)	30	45	60
Plate material	aluminum	-	steel
(Plate mass)	(Low)	-	(High)
Anvil plate material	none	aluminum	steel
Insulator layer	none	-	polymeric
Bullet velocity (m/s)	low	medium	high

Below is a summary of the rationale behind the selected factors and their levels:

- **Bullet mass** is varied by adjusting the bullet's body length. It ranges from 0.2 kg to 1.0 kg, the upper limit being defined by the design capacity of the test bench. The mass of the bullet changes the momentum at impact.
- **Bullet material** is tested across three variants: PLA, aluminum, and steel. This selection allows for assessing how tip hardness affects impact behavior and content in the force spectrum.
- **Bullet tip radius** is varied from 30 mm to 60 mm to explore how contact geometry influences key parameters of impact such as contact duration and maximum force.
- **Plate material** is tested using steel and aluminum, to examine how the stiffness, damping and mass characteristics of the target affect wave propagation and contact force profiles.
- **Anvil plate material** is set on two levels to see if significant difference in the response is registered depending on stiffness and damping of the material
- **Insulator layer** is included since the presence of a damping polymeric material can be used to change the characteristic of the force profile and ultimately the SRS of the plate.

- **Air tank pressure** is swept across the entire operational range of the compressor. This ensures the experiment spans the full range of impact velocities, capturing both the lower and upper bounds of the loading conditions.

These choices result in a balanced yet comprehensive DOE, designed to capture the interplay between material, geometric, and dynamic parameters in the context of impact mechanics. Due to a dependency between certain variables, specifically, the insulating layer can only be applied when the anvil plate is present, the total number of possible configurations is calculated as:

$$2 \cdot 3^4 \cdot (3+2) = 810\, tests \tag{3.1}$$

This extensive test matrix is not feasible, particularly given the need for repetitions to ensure statistical reliability of the acquired data.

To mitigate this, the total number of tests can be reduced using Latin Hypercube Sampling (LHS), a method known for efficient space filling sampling of the input space [46]. LHS is especially effective at capturing nonlinear effects even with a reduced dataset [47]. The number of treatments can be tailored to the available experimental resources, making LHS particularly convenient.

Unlike full-factorial designs, a LHS does not exhaustively enumerate every combination of factor levels; instead, a tradeoff between the interaction coverage and the number of runs must be found. A recommended initial size for DOE with up to ten parameters is between 10 and 15 times the number of dimensions [48, 49]. This ensures each factor is sampled in many different combinations, making it likely to detect a interactions between them. For example, given $n = 15 \times d$ tests across d dimensions, an $n \times d$ matrix is generated, where each dimension is divided into n equally spaced levels. Each sample is constructed such that each level is used exactly once per dimension [50]. An intuitive representation is given by Montgomery for a 2D case, which is a Latin Square: this problem is closely related to sudoku in which each rows and column must contain all the numbers without repetitions. The main drawback of LHS can be computationally intensive compared to factorial designs, tools such as MATLAB's `lhsdesign` function streamline the process. Using this function, a reduced yet representative campaign of 105 (15 times the number of dimensions) tests was generated, the complete design is shown in Appendix A.

Chapter 4

Contact Mechanics

In this chapter, the methodology used to develop a data-driven model based on experimentally measured impacts is presented. The structure of the chapter follows the sequence illustrated in Figure 4.1. At first an overview of the main characteristics of the experimental dataset is presented. Subsequently, the feature extraction process from each time series,represented by the orange block in Figure 4.1, is described. This process leads the the creation of a database on which a ML algorithm is trained and validated (green block) to obtain a fully data-driven contact force model.

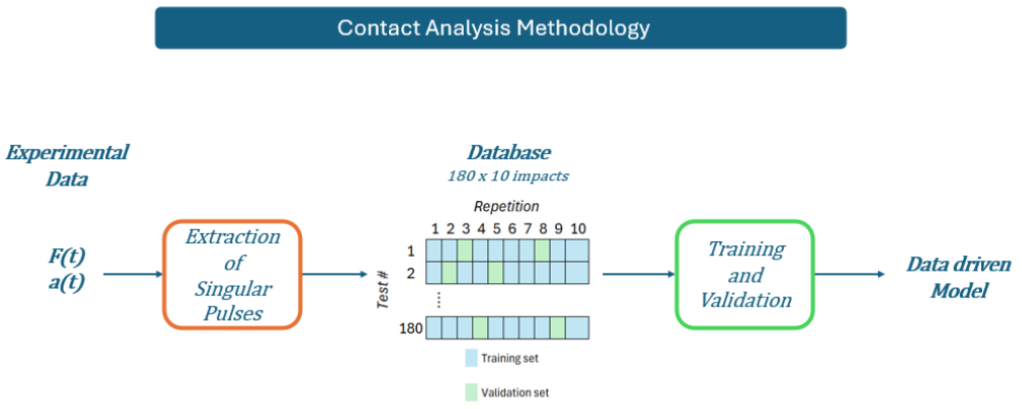

Fig. 4.1 Overview of the methodology

A fundamental step in developing any machine learning model is the creation of a robust and comprehensive dataset that captures the key characteristics of the physical phenomenon under investigation. In this study the dataset described in

[39] is used. It comprises pulses generated by an instrumented impact hammer with interchangeable tips, striking a resonant plate made of Al6061. The plate features an intentionally irregular geometry, specifically designed to avoid symmetry related artifacts that could bias the results and compromise the model's generalizability. The data used in this study includes force signals recorded by a load cell (Dytran Dynapulse 5800B4) placed at the front of the hammer, as well as acceleration signals captured by a charge accelerometer (B&K 8309).

The dataset is designed to comprehensively capture the dynamics of shock events. To ensure a balanced exploration of all relevant variables, a full factorial DOE is employed. This method provides an optimal trade off between the total number of tests and the ability to isolate and analyze the influence of each parameter independently. Six parameters are systematically varied: the impact position (which plays a critical role in SRS calculation but has a lesser effect on the mechanics of the impact itself) hammer speed, hammer tip type, material of the anvil plate, presence of an insulating layer between hammer and anvil, and the boundary conditions of the resonant plate. Each of these parameters is tested at multiple levels, as detailed in Table 4.1.

Table 4.1 Experimental factor levels

Factor Name	**Low-level**	**Mid-level**	**High-level**
Impact position (input)	#1	#2	#3
Hammer speed	Low	-	High
Hammer head material	Aluminum	Delrin	Polyurethane
(Radius in mm)	(30)	(30)	(15)
Anvil plate material	None	Aluminum	Steel
Anvil insulator	None	-	Polymeric
Plate boundary conditions	Free	-	Fixed

It is important to note that the hammer speed is controlled manually by the operator and, therefore, only defined at two nominal levels. This introduces some variability between tests. To enhance the statistical robustness of the analysis, each of

the 180 unique configurations is repeated over 10 impacts, resulting in an statistically significant dataset for model training and validation.

The material properties used in this study, required for modeling and feature construction, are sourced from the Ansys Granta material database [51]. A summary of these properties is provided in Table 4.2.

Table 4.2 Material properties used in the study

Material	$E\ (GPa)$	$\nu\ (-)$	$\rho\ (kg/m^3)$	$\sigma_y\ (MPa)$
Aluminum	69.9	0.33	2700	276
Steel	200	0.30	7800	400
Delrin	3.20	0.35	1410	71.7
Polyurethane	0.03	0.39	1210	51.0

4.1 Processing of the database

First, the input signals are pre-processed to remove noise. Ideally, the accelerometer signal would directly reflect the dynamics at the impact plane. However, since mounting the sensor directly on the hammer tip is unfeasible, the signal is significantly influenced by the hammer head structure. After impact, the acceleration information must travel the length of the hammer head before reaching the sensor. As a result, even though force and acceleration are acquired synchronously, a measurable delay between the two signals can still occur. To ensure that this delay is solely due to the physical distance between the contact plane and the sensor, the wave propagation time was estimated following the approach in [52]. The propagation velocity of the compression waves,

$$u_{wave} = \sqrt{\frac{E}{\rho}} \tag{4.1}$$

The time required for the wave to reach the back of the hammer is $t = 1.24 \cdot 10^{-5}\ s$, which is comparable with the sampling period $T_s = 1.9531 \cdot 10^{-5}\ s$, so, discrepancies of up to 2 samples between force and acceleration have been considered acceptable.

In addition to the delay, the hammer body alters the signal according to its own dynamic behavior. This behavior can be characterized by estimating the system's transfer function (tf) using the MATLAB command `tfestimate`, with acceleration

as the output and force as the input. Once the transfer function, $\mathrm{tf}(\Omega)$, is identified, the influence of the system can be removed by deconvolving the output signal in the frequency domain:

$$a_{clean}(\Omega) = \frac{a(\Omega)}{\mathrm{tf}(\Omega)} \tag{4.2}$$

Finally, the cleaned signal is converted back to the time domain using the inverse Fast Fourier Transform (ifft).

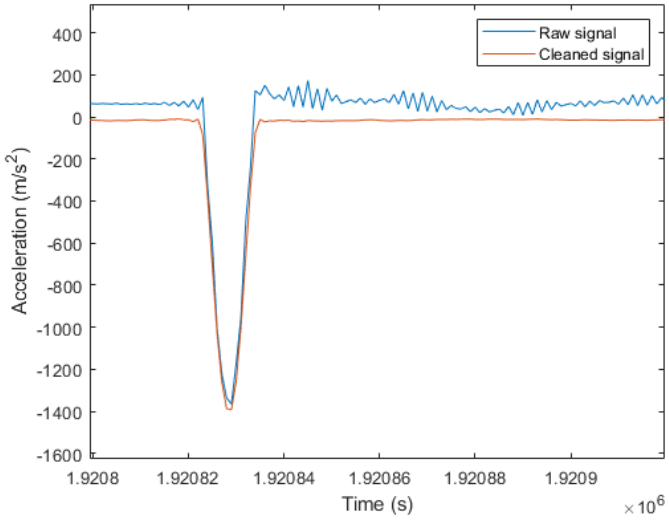

Fig. 4.2 Effect of the deconvolution on the acceleration signal in time domain for a randomly selected impact

As shown in Figure 4.2, this method effectively removes the bias and post-impact oscillations introduced by the hammer body. Starting from the blue signal (raw acceleration) as input, the process yields the orange signal (cleaned acceleration) as output.

Once the cleaned acceleration signal has been extracted for each of the 180 tests, the next step is to isolate ten individual pulses per test. To achieve this, two different approaches are proposed and compared. In both methods, the force signal is used to identify and segment the full acquisition, as it exhibits less noise after pre-processing. Meanwhile, the acceleration data is employed to estimate velocity via numerical integration.

The first approach involves detecting the locations and amplitudes of the ten main peaks in the force signal. For each peak, a search is conducted to the left and right to

determine the corresponding time window in which significant activity occurs. This search continues while the signal amplitude remains above a threshold, specifically, 0.5% of the peak value. When the amplitude falls below this threshold, the first and last instants of contact are identified. This method is illustrated in Figure 4.3a.

The second approach adopts a "force window" strategy. In this method, all portions of the time series where the force is below a defined threshold (0.5% of the peak force) are set to zero. A logical (Boolean) vector is then created to indicate where the force values are nonzero. By applying the `diff` function to this vector, the starting and ending indices of each pulse, corresponding to contact events, can be identified. This process is illustrated in Figure 4.3b.

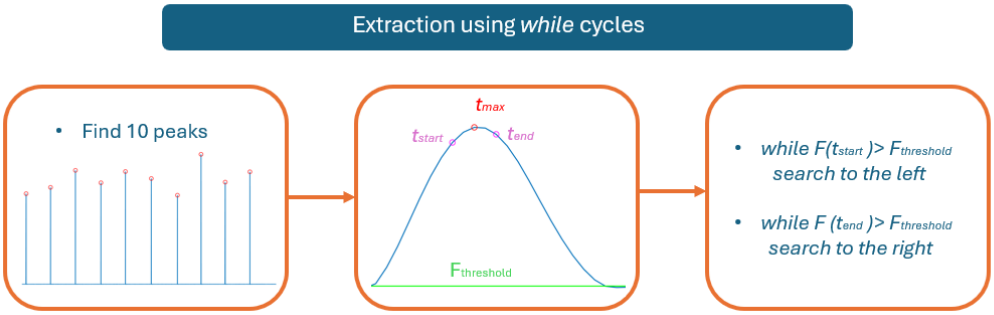

(a) While cycles

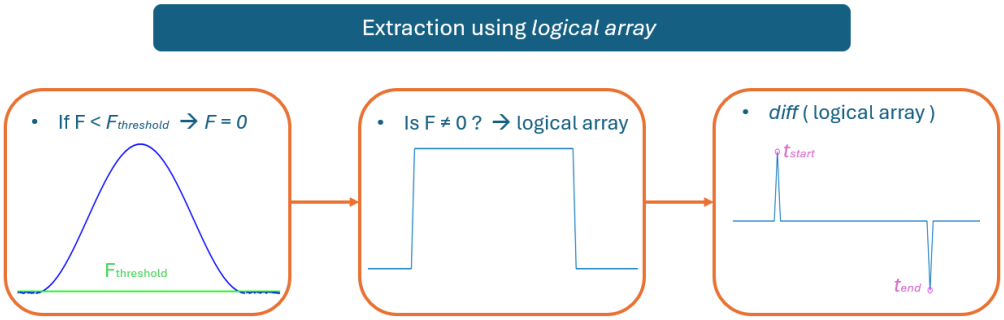

(b) Logical array

Fig. 4.3 Proposed methods to isolate the information contained in the experimentally acquired time series

For both methods, a cubic smoothing spline interpolation is applied to each pulse, as the number of samples during contact is often very limited, particularly when using the aluminum tip. This occurs despite the sampling period T_s being on the

order of 10^{-5} s due to the total contact time being approximately 10^{-4} s. The spline interpolation allows for the estimation of force values on a finer time grid, with ten times the resolution of the original. The same procedure is applied to the acceleration signal, which significantly improves the accuracy of the estimated impact velocity through numerical integration.

To verify that the resampling does not introduce significant errors into the analysis, the Root Mean Square Error (RMSE) is computed between the original signal and the interpolated signal at the original time points.

$$RMSE = \sqrt{\frac{\sum_{i=1}^{n}(F - F_{interpolated})^2}{n}} \tag{4.3}$$

Where n is the number of samples in the original signal. In addition the RMSE has been normalized against the range of the signal, in this case since the minimum force is very close to zero the Normalized RMSE (NRMSE) can be seen almost as a percentage error between the real and the interpolated data.

$$NRMSE = \frac{RMSE}{F_{max} - F_{min}} \tag{4.4}$$

where:
- $F_{max} = max(F(t))$
- $F_{min} = min(F(t))$

As shown in the heatmap in Figure 4.4, no error is introduced by interpolation of the signals. The error remains very low, consistently below 0.5%, and is primarily concentrated in the tests conducted with the aluminum hammer tip, where fewer than 10 samples are often recorded during contact. Notably, a periodic pattern in the error distribution emerges, corresponding to the changes in hammer tip material throughout the testing sequence. For example, in the first 18 tests, groups of six tests show a clear alternation in error magnitude that aligns with the sequence of hammer materials: initially aluminum, with the fewest samples and highest error, followed by Delrin, and finally polyurethane (with the most samples and therefore the smallest discrepancy between the raw and interpolated signals).

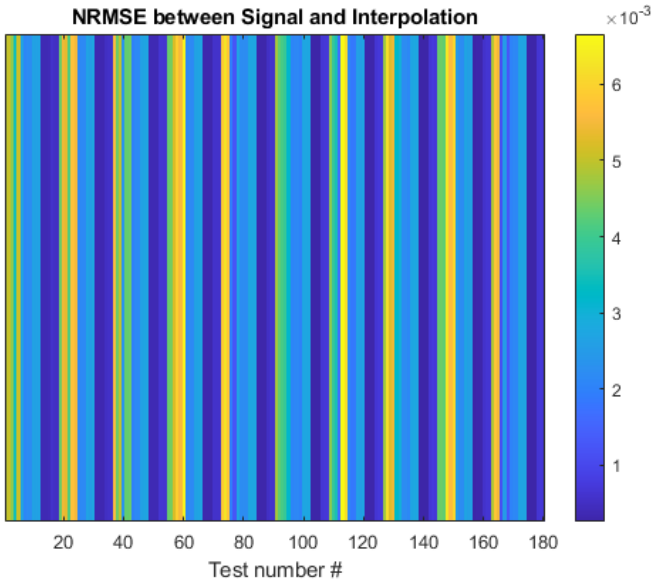

Fig. 4.4 NRMSE between acquired force signal and interpolated one

The effect of interpolation can be clearly visualized by examining the force signals in the three different cases shown in Figure 4.5. When the number of samples is low, as with the aluminum hammer tip, the cubic spline interpolation significantly smooths the pulse, enhancing its definition across the time domain and improving the accuracy of momentum computation. As the number of samples increases, such as with Delrin, the benefit of interpolation diminishes. In the case of polyurethane tips, where sample numbers are the highest, the original signal is already well resolved, and the effect of interpolation becomes negligible.

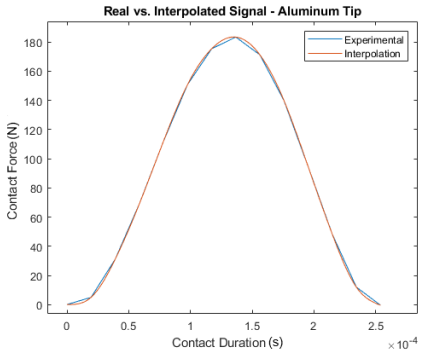

(a) Case a - Aluminum Tip

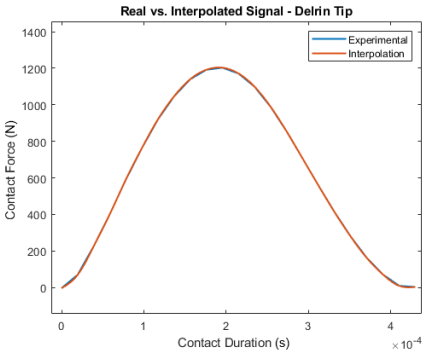

(b) Case b - Delrin Tip

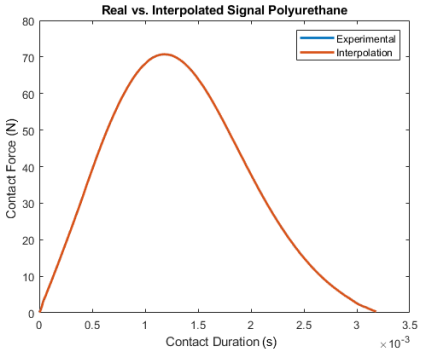

(c) Case c - Polyurethane Tip

Fig. 4.5 Difference between the experimentally acquired and interpolated force signal, three randomly selected impacts each with different materials

To determine the most appropriate windowing method to continue the analysis, the results from each approach are compared. The difference in selected contact duration τ, between the two algorithms is computed as in Eq. 4.5:

$$Percentage\ difference = \frac{\tau_{while} - \tau_{logical}}{\tau_{while}} \cdot 100 \tag{4.5}$$

Tests 1, 40, and 109 exhibit the largest discrepancies, with nearly a 12% difference in the extracted contact times, as shown in Figure 4.6.

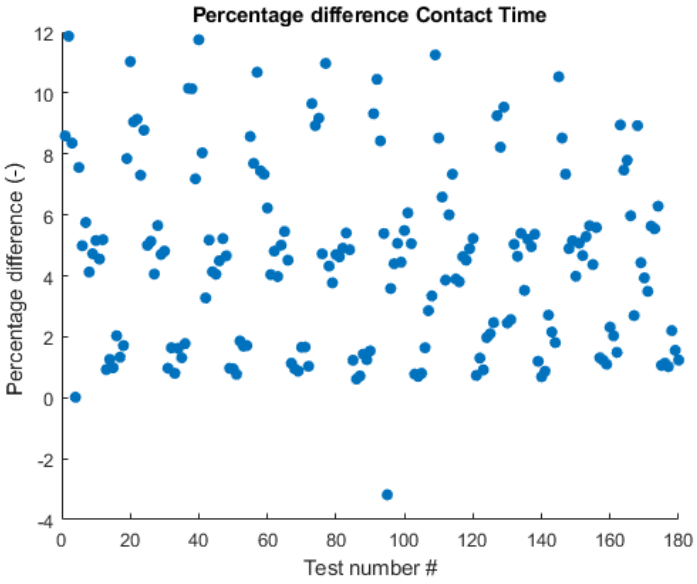

Fig. 4.6 Perceptual differences in contact duration due to different extraction methods

To establish which of the two methods is better performing the signal acquired in test number 1 is manually windowed and plotted in Figure 4.7 as a blue dashed line. In the same graph the portions of signal automatically selected are superimposed: the continuous red line is the result from the while cycle and the green line is from the logical operator extraction. It is clear how the red line closes matches the manually obtained results, meanwhile, the green one gives a short estimate. Under the assumption that the best performing model in this worse case is the overall best performing, the *while cycle* extraction is chosen.

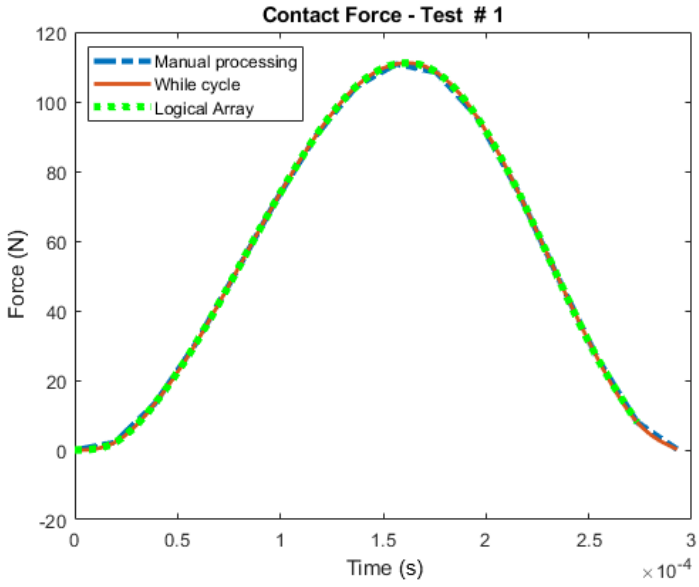

Fig. 4.7 Comparison of automatic and manual extraction - Test number 1

4.2 Selection of Inputs and Outputs of the models

The objective of this model is to predict the force evolution during contact in the time domain, effectively creating a digital twin of the experimental test bench. To achieve this, a set of input parameters must be selected. These parameters should contain sufficient information to enable the learning models to identify the influence of each factor contributing to the observed phenomena.

4.2.1 Inputs

As demonstrated by Hertz, key factors influencing contact time and the force exchanged between bodies include geometry, material properties, and the kinematic variables of the impact. The full factorial dataset is designed to capture the influence of all the factors listed in Table 4.1. Among these, the factors shown in Table 4.3 have been selected as inputs for the machine learning models.

Table 4.3 Predictor chosen as inputs for the machine learning models

Predictors for Machine Learning models	
Bullet	$R_s\ E_s\ \nu_s\ \rho_s\ \sigma_{y,s}\ u_i$
Plate	$E_p\ \nu_p\ \rho_p\ \sigma_{y,p}$
Anvil Plate	none / aluminum / steel
Polymeric Insulator	present / not present
BCs	free-free / fixed

The selected material properties of the plate correspond to the first layer of material that the bullet impacts: aluminum when no anvil plate is used, and steel or aluminum when the anvil is present. While the presence of the anvil plate is partially accounted for in the material properties predictor, a separate parameter is still used to distinguish between the cases of aluminum contact on an anvil or resonant plate. Although the mass of the impacting body could provide additional insight, the database was created using only one hammer, so no information is available regarding the effect of mass variation.

To identify potential redundancies in the set of predictors, the correlation between them was computed and is presented in Figure 4.8. Young's modulus, Poisson's ratio, and the yield strength of both the plates and hammer tips show the highest correlations, with values close to ± 1. However, these factors are not redundant. This high correlation arises because only two materials, steel and aluminum, were used in the study, and these materials exhibit consistent trends: all parameters increase or decrease together as one moves from one material to the other. With the inclusion of additional materials with intermediate mechanical properties, the correlations between these predictors would likely decrease, making it easier to distinguish their individual contributions.

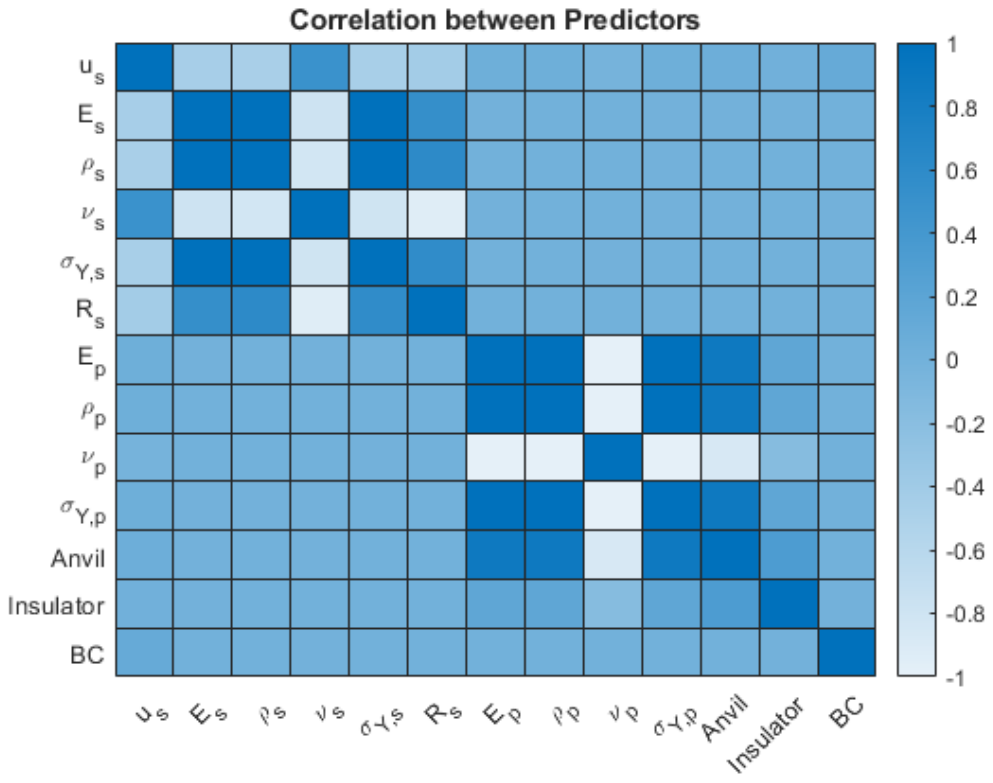

Fig. 4.8 Correlation between the inputs of the ML models

4.2.2 Outputs

At first glance, it might seem convenient to characterize each output using a set of physical quantities, such as maximum force, impulse, contact duration, or time of contact. However, relying on these parameters alone complicates the problem of reconstructing the full time evolution of the force signal. One potential approach would be to predefine a function describing the overall shape of the force curve and then scale it to fit each specific case. However, this strategy lacks flexibility and limits the model's generalization capability. For these reasons, the desired outputs of this study are time series representing the contact force during impact events. Since variations in material properties and initial motion conditions lead to differences in the duration of these time series, it is crucial to apply time normalization. This step ensures that machine learning models can consistently learn from and effectively capture key characteristics of the signals, such as their shape and amplitude.

By resampling each force signal to 20 equidistant points (dividing the contact event into ventiles), the model can learn the evolution of force over a normalized cycle, independent of the actual contact duration. Twenty points are deemed the correct number in order correctly resolve force evolution without a large expansion from the 13 input parameters. This decoupling of spatial and temporal variability is a well established practice in fields such as gait analysis[1] [53], biological signal analysis [54], and other applications involving variable length signals.

Once shape and amplitude are modeled independently of time, a second model can be trained to predict the total contact duration from the same set of input features. Combining both predictions allows reconstruction of the original time series in physical time units.

To this end, interpolation of the signals carried out in Section4.1, revealed that the contact force profiles are well approximated by cubic smoothing splines. These are functions with continuous first and second derivatives, which minimize a penalized residual sum of squares [55].

$$RSS(f,p) = \sum_{i=1}^{N} \{y_i - f(x_i)\}^2 + (1-p) \int f''(t)^2 dt \tag{4.6}$$

Where p is a smoothing parameter and N is the number of elements of the vectors to interpolate. In this context, the vector x contain the temporal information, i.e., the contact duration, while the vector y contains the predicted evolution of contact force over time. Specifically, y is the 20 element vector output by the machine learning model, representing the normalized force profile.
Such interpolation can be easily implemented in MATLAB using the function `csaps(x,y,p)`.

The time vector x is generated starting with the scalar contact time estimation, τ. To perform the cubic spline interpolation it is necessary to have the same number of element in x and y: since the points of y are 20 equidistant moments in the contact duration, the same is applied to the time vector. Using `linspace` a 20 element vector spanning from time instant 0 to time τ is generated, thus reconstructing the time axis in physical units. This step effectively maps the force evolution from normalized space back into real time.

[1]The action of walking, involving the coordinated motion of multiple joints and muscles in the musculoskeletal system

Figure 4.9 summarizes how the proposed approach involves training two separate models: a multivariate model to predict the 20 elements force vector, and a univariate model to estimate the total contact duration used to create a 20 elements time vector. These two outputs are then combined using the MATLAB function `csaps` to reconstruct the complete time resolved force profile.

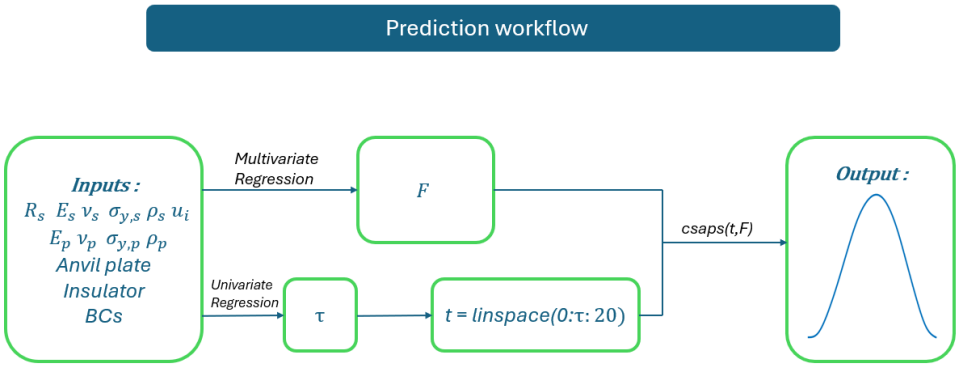

Fig. 4.9 Steps of the machine learning algorithm to find force evolution in time domain

4.3 Models

Before starting the optimization procedure, some different types of regression are carried out to see which one yields to the most accurate predictions. The dataset is divided into training and validation sets to train and assess the performance of each model. Specifically, 80% of the pulses (1,440 samples) are allocated for training, while the remaining 20% (360 samples) are reserved for validation. To ensure an unbiased evaluation, the validation set is constructed by randomly selecting 2 out of the 10 repetitions from each test. This randomized selection minimizes the risk of systematic errors, such as operator fatigue or other time dependent effects during the later repetitions, influencing the results. Furthermore the evaluation is more robust since the models are tested on every possible combinations of factors of the full factorial dataset.

4.3.1 Contact time prediction

Since predicting the contact time is a univariate regression problem, the `regression Learner` app in MATLAB was used to train various models and identify the best performing. The evaluation metric used is absolute error computed between the actual and predicted contact time τ over the entire validation set and then averaged.

$$err = \frac{1}{n}\sum_{i}^{n} \frac{|\tau_{i,actual} - \tau_{i,predicted}|}{\tau_{i,actual}} \tag{4.7}$$

Among the tested models presented in Table 4.4, the best performance was achieved by a decision tree with a minimum leaf size of 36, resulting in an error of 0.0581 . Decision Trees operate by partitioning the predictor space into a series of rectangles and assigning a simple output model, typically a constant value, to each region. While effective, this approach can make the prediction quality highly sensitive to the training dataset. For this reason, a Gaussian Process Regression (GPR) model was chosen. GPR yielded the second best error ($err = 0.1132$), and offers the added advantage of greater generalization, which is particularly beneficial given that the same regression type is well suited for the subsequent force prediction task.

Table 4.4 RMSE for each time prediction model

Rank	**Model Type**	***err* (-)**
1	Tree	0.0581
2	Gaussian Process Regression	0.1132
3	Ensemble	0.2292
4	SVM	218.29
5	Kernel	234.79
5	Linear Regression	1536

4.3.2 Force prediction

For what concerns the force vector the selected models include neural networks, linear regression, Support Vector Machine (SVM) regression, and kernel regression, also in this case all of them have been trained in MATLAB using built in functions.

Given a function that has p variables, linear methods approximate the response $f(X)$, as follows [55]:

$$f(X) = \beta_0 + \sum_{j=1}^{p} X_j \beta_j \tag{4.8}$$

where.
- β_0 is the bias, the value which $f(X)$ assumes when all inputs are nil.
- X_j is the j^{th} predictor variable (feature) in the input vector X.
- β_j is the coefficient associated with the j^{th} predictor X_j, representing the contribution of X_j to $f(X)$.

As it has been done in this case, the model can be expanded to use combinations of X, X^2, X^3 enabling to capture more complex relationships. MATLAB's `mvregress` function was used. Additionally, Partial Least Squares (PLS) Regression was employed using the `plsregress` function. PLS Regression identifies correlations between inputs and outputs while simultaneously considering the variance of both, making it suitable for multivariate regression tasks where predictors are highly collinear [56].

Since analytical models for contact mechanics are notoriously non-linear , kernel regression and support vector regression were also implemented. Unlike the aforementioned global methods, kernel regressions, make local regressions, meaning that training data is stored and predictions are made looking at the closest neighbors of the given input. To decide the amount of influence of each neighboring point the kernel function K is used. With the command `firtrkernel`, K is defined as a Gaussian function with variance λ:

$$K = \frac{1}{\lambda} exp\left[-\frac{||x - x_0||^2}{2\lambda}\right] \tag{4.9}$$

where:
- x is the point in the input space where the kernel is evaluated.
- x_0 is the center or reference point of the kernel.
- $\|x - x_0\|^2$ is the squared Euclidean distance between x and x_0.

Once the weights are established by the kernel, the regression function is computed and optimized using both linear regression through ordinary least squares and

a Support Vector Machine regression. Another model that provides a local regression is the GPR, implemented in MATLAB as (`fitrgp`). GPR particularly indicated to find and capture complex, non-linear relationships between the inputs. Additionally, it provides uncertainty estimates on the predictions [57, 58].

It is important to underline that training of the aforementioned kernel models in MATLAB is limited to univariate cases, for these reasons 20 different models, one for each element of the force vector, have been trained. While this approach ensure accurate predictions, it significantly increases the computational time.

The final category of non-linear models selected for this study consists of Neural Networks (NNs). NNs are powerful tools for capturing non-linear relationships in data without requiring explicit assumptions about the underlying functional forms of the relationships between the input features and the output response [59] . This flexibility makes NNs highly suitable for modeling complex systems. However, one significant drawback of NNs is their lack of interpretability the internal mechanisms behind their predictions are often considered a "black box," making it challenging to explain the rationale behind their outputs in practical applications.

For this study, a total of five different NNs models were trained and validated to investigate the impact of key hyperparameters on performance. The hyperparameters explored included the number of perceptrons in each layer and the number of hidden layers in the architecture. All the trained models utilized the Rectified Linear Unit (ReLU) activation function, which is commonly used due to its computational efficiency and ability to mitigate the vanishing gradient problem encountered during training [60] . Furthermore, this kind of activation is found to yield more accurate predictions than sigmoid and tanh [61, 62], with the added value of being the most computational efficient.

The models are evaluated by computing the NRMSE, as defined in Equation (4.4), for each of the 180 pulses and then averaging the results. Among the initial models, Gaussian Process Regression yields the highest accuracy, with a mean NRMSE of approximately 0.0464. The performance of each model across the impact cases is visualized in Figure 4.10, while Table 4.5 provides a summary of the mean RMSE and NRMSE values over the entire validation set. From the heat map it is evident NNs models, especially those with three layers and more neurons per layer, exhibit consistently low NRMSE values across nearly all test cases. This indicates enhanced generalization ability across the dataset. Gaussian process regression shows

consistently small errors, though some periodicity is noticeable, likely due to the variation in tip material properties. Conversely, the expanded linear regression and partial least squares regression models show consistently high errors and pronounced periodicity patterns, highlighting their limited generalization capabilities and inability to adapt to changes in the dataset.

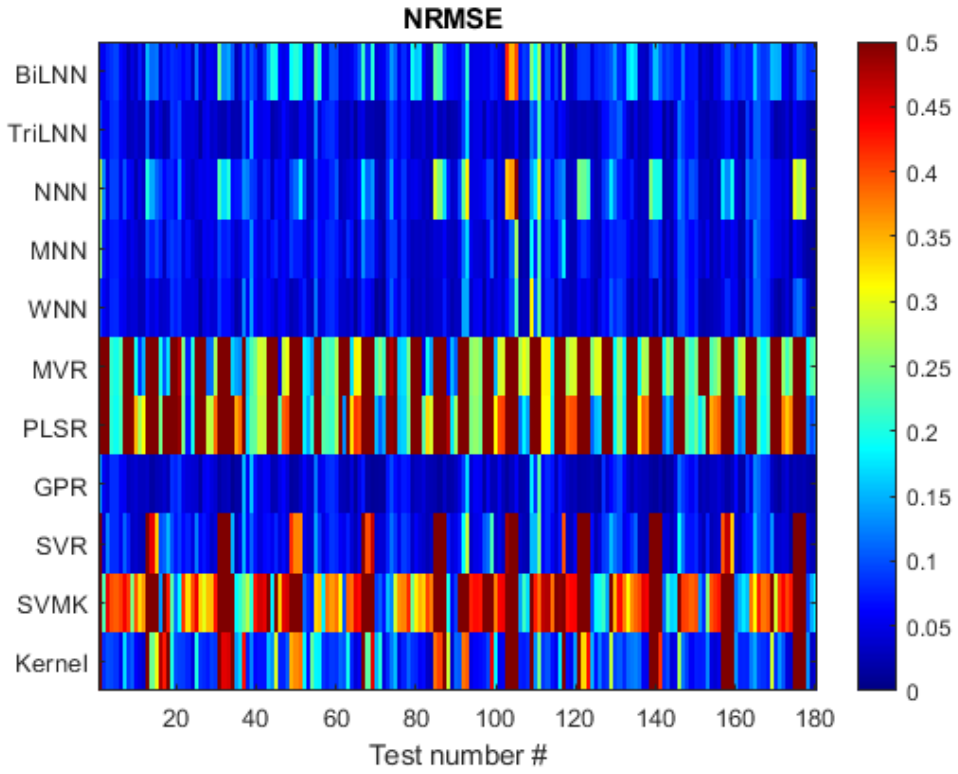

Fig. 4.10 NRMSE comparison of each of the considered force regression models. From the top: bilayer, trilayer neural networks, narrow, medium, wide neural networks, multivariate linear regression, partial least square regression, gaussian process, support vector regression, support vector machine kernel, kernel regression.

Table 4.5 Mean RMSE and NRMSE of each force regression model

Rank	Regression Type	mean RMSE (N)	mean NRMSE
1	Gaussian Process	34.624	0.046397
2	Trilayered NN	34.730	0.049030
3	Wide NN	35.645	0.055375
4	Coregional GPR	35.882	0.057832
5	Medium NN	36.831	0.061737
6	Narrow NN	42.106	0.092828
7	Bilayered NN	49.820	0.095664
8	Support Vector	45.911	0.160440
9	Kernel	71.379	0.236350
10	Multivariate Linear	279.91	0.993200
11	Support Vector Kernel	287.40	1.020200
12	Partial Least Square	303.76	1.472600

In this particular application the algorithms are required to produce 20 pieces of information starting with 13 inputs, according to findings in the literature [63, 64], gaussian process regression is particularly well suited for problems where the input dimensionality is lower than the output dimensionality. These findings align with the results presented in Table 4.5. In particular, since each of the 20 points describing force evolution is likely correlated to the others, a coregionalization Kernel can be very effective in making predictions. MATLAB does not support true multivariate GPR or coregionalization, so, instead of training a separate model for each element of the output vector, a fully multi output GPR model was implemented and optimized using the GPyTorchTorch library [65]. In parallel, a NN was also considered, as its performance (NRMSE = 0.049) closely approaches that of the GPR model.

4.4 Optimization

Following the selection of the most appropriate regression models, a hyperparameter optimization procedure is performed to improve the performance. Given that three different models are used, model specific optimizations are employed, with model specific objective functions.

The models include:

1. A Neural Network for force prediction combined with a Gaussian Process regression for time prediction, both developed in MATLAB.
2. A multi output GP regression with a coregional kernel for predicting the force vector and a single output GP regression for time prediction, both implemented using the GPyTorchTorch library in Python.

In MATLAB, Bayesian optimization is employed to tune several key hyperparameters of the GP models. These include the choice of kernel function, which influences the model's flexibility in capturing smooth or abrupt variations in the data; the basis function, which sets the prior mean of the process and can be constant, linear, or zero; the noise standard deviation (sigma), and the standardization setting, which determines whether the input features are normalized before training, a step that often improves numerical stability and convergence, particularly in the presence of features with differing scales like in this study. The optimization process is limited to 30 iterations to balance computational efficiency with performance improvement as suggested by Matlab documentation.

The Python based models rely on the built-in optimization routines provided by the library. These routines automatically optimize the kernel structure and its associated parameters, such as:

- Variance, which controls the overall amplitude of the GP prediction.
- Covariance that controls how the output amplitude varies in relation to each other.
- Lengthscale, determining how quickly the output changes as a function of inputs.
- Noise, determining the level of confidence of each prediction.
- Standardization is always applied to the training set.

In contrast, the hyperparameters of the NNs are optimized using a Genetic Algorithm (GA). This choice is supported by findings in literature, which highlight the GA as one of the most effective methods for tuning neural network architectures

[66]. In this context, several key hyperparameters are subject to optimization. The number of neurons per layer and the number of hidden layers are adjusted to control the representational capacity of the network, balancing complexity with generalization.The regularization parameter λ is also tuned; this value penalizes overfitting by constraining the magnitude of the network weights. The number of folds for k-fold cross validation is set to 5, in this way 288 impacts out of the 1440 of the training set are used to perform a cross validation, enhancing the robustness of the regression. The GA itself is configured following standard practice, with an initial population size of 50 individuals and a maximum of 200 generations, as recommended by MATLAB documentation but the optimization is stopped at 50 generations since the solution is already convergent.

A summary for the hyperparameters and the performance of each model after optimization is reported in the Tables 4.6, 4.7, 4.8, 4.9.

GP regression for Time prediction - GPyTorch
Exponential Quadratic Kernel
Variance = 0.77
Lengthscale = 13
err = 0.0430

Table 4.6 Optimized Hyperparameters Gaussian Process for Time prediction in GPyTorch

GP regression for Force prediction - GPyTorch
RMSE = 35.851 N
NRMSE = 0.048

Table 4.7 Optimized Hyperparameters Gaussian Process for Force prediction in GPyTorch

GP regression for Time prediction - MATLAB
Sigma = $4.25 \cdot 10^{-4}$
no Basis function
ARDMatern32 Kernel
Standardization on
err = 0.0430

Table 4.8 Optimized Hyperparameters Gaussian Process for Time prediction - MATLAB

NN regression for Force prediction - MATLAB
2 hidden layers
144 neurons per layer
Lambda = 0.2009
RMSE = 34.481 N
NRMSE = 0.0479

Table 4.9 Optimized Hyperparameters Neural Network Force prediction - MATLAB

Chapter 5

Results

In this chapter the results of the thesis are presented and discussed starting with the analysis of the velocity prediction model and continuing on the contact model.

5.1 Validation of velocity prediction model

In this section, the scaled adiabatic expansion model presented in Chapter 2 is validated by comparing its muzzle velocity predictions to laser measured velocities at five different chamber pressures. For each test condition, the model predicted velocity $u_{s,\text{predicted}}$ is computed and then compared to the corresponding laser measured value $u_{s,\text{measured}}$ using the percentage error:

$$e = \frac{u_{s,measured} - u_{s,predicted}}{u_{s,measured}} \cdot 100 \tag{5.1}$$

where a negative e indicates model over prediction. Each measured velocity is reported with its associated uncertainty, calculated following the Guide to the Expression of Uncertainty in Measurement (GUM) [67]:

$$\Delta u_s = \sqrt{\left(\frac{\partial u_s}{\partial L}\Delta L\right)^2 + \left(\frac{\partial u_s}{\partial t}\Delta t\right)^2} = \sqrt{\left(\frac{1}{t}\cdot\Delta L\right)^2 + \left(\frac{-L}{t^2}\cdot\Delta t\right)^2} \tag{5.2}$$

where:
- $u_s = L/t$ denotes the measured muzzle velocity.

- $\Delta L = 1$ *mm* corresponding to the meter resolution.
- $\Delta t = 4 \cdot 10^{-5}$ *s* corresponding to the 25 kHz sampling rate used during the experiments.

Table 5.1 summarizes, for each pressure, the laser measured and model predicted velocities, their uncertainties, and the resulting errors.

Table 5.1 Comparison of predicted and measured bullet velocities, uncertainties in are computed via Eq. 5.2

Test #	**Pressure (bar)**	**Measured u_s (m/s)**	**Predicted u_s (m/s)**	e (%)
1	0.2319	10.37 ± 0.13	10.58	-2.1
2	0.2651	11.87 ± 0.15	11.35	4.4
4	0.4042	13.80 ± 0.18	14.13	-2.4
5	0.5784	16.35 ± 0.23	16.98	-3.9
3	0.6158	18.97 ± 0.28	17.53	7.6

The correction factor $\eta = 0.5$ introduced in Chapter 2 confines the prediction error to below 8 %. This reduction in muzzle velocity is primarily attributed to mass flow rate leakage between the projectile and barrel inner walls. Corner [68] proposes a dimensionless leakage parameter ψ, where $\psi = 0$ denotes a perfect seal and $\psi = 1$ indicates full blow by of the expanding gases. In conventional firearms, an interference fit, where a soft metal bullet housing deforms against a hardened steel bore, minimizes ψ; however, the pneumatic launcher employed here features a radial clearance of 0.5 mm and thus operates in a high leakage regime. The ratio of actual to ideal exit velocity can be approximated as function of ψ:

$$\frac{u_s}{u_{s,no\ leaks}} \approx (1-\psi)^{0.7} \tag{5.3}$$

For large leakage systems such as this pneumatic gun, ψ typically lies between 0.4 and 0.6. Substitution into Eq. 5.3 predicts velocity reductions of approximately 30 % to 47 %, in agreement with the experimental measurements and the findings of Cave [44].

Figure 5.1 presents the chamber pressure trace overlaid with the laser detection signal. While the laser sensor voltage output can be converted to distance, this

is unnecessary for the current application. The key requirement is to accurately determine the time the projectile passes the sensor, not its exact position. Therefore, the signal is used directly in volts without post-processing.

After impact on the resonant plate, the projectile rebounds slightly, causing the trapped air to behave as a SDOF mass spring system. In all five tests, despite rebound, no instances of multiple impacts are observed, underscoring the efficacy of the radial vent holes in preventing pressure buildup behind the projectile.

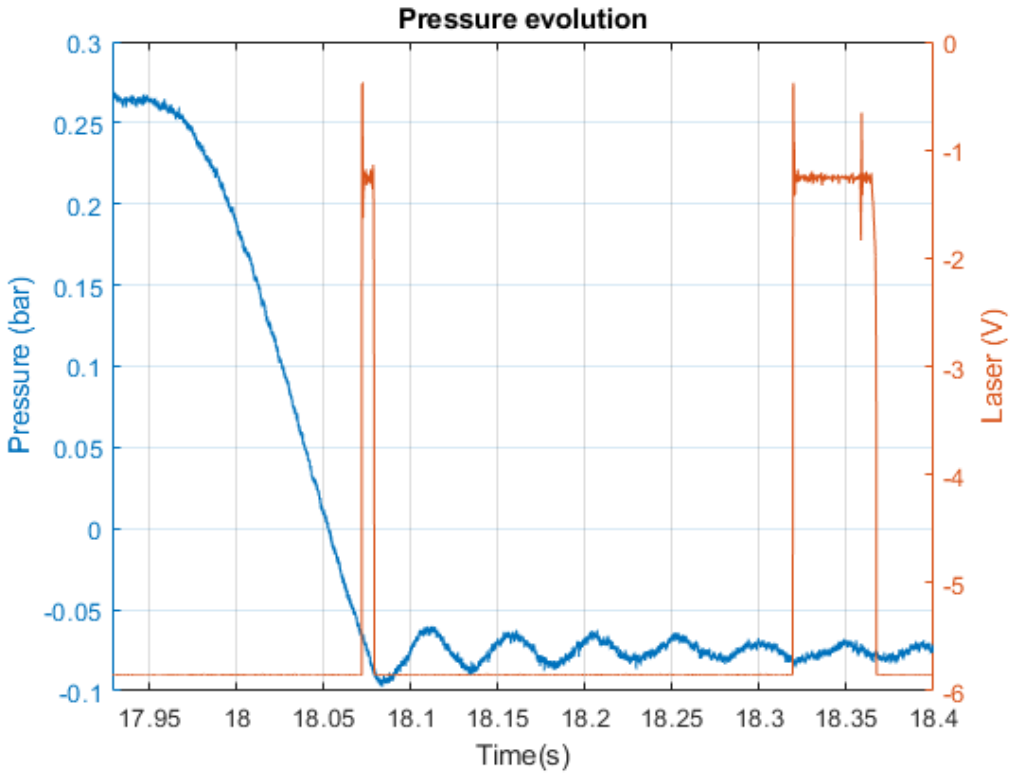

Fig. 5.1 Measured pressure evolution for test 2. The laser signal is used directly in volts since only passage time is needed and not the distance of the object.

Transient negative pressure excursions are observed in the chamber pressure trace. Such depressions may arise from pressure transducer calibration errors or, more plausibly, from rapid valve closure. According to Bernoulli's principle, abrupt interruption of a high speed flow converts the dynamic head, $\frac{1}{2}\rho u_s^2$, into a local depression, which is register within the tank. The flow induced depression hypothesis is supported by the close agreement between predicted and laser measured velocities when applying the same leakage correction factor reported in [44]. Nevertheless,

additional tests, ideally varying valve opening time, are required to conclusively rule out instrumentation artifacts.

Figure 5.2 superimposes the experimental velocity data on the model prediction incorporating $\eta = 0.5$. For this limited dataset, the model exhibits high fidelity, with a mean absolute percentage error of $|e| = 4.07\%$, thereby validating its predictive capability. It should be noted that the leakage correction parameter η may vary with barrel wear, slug diameter, and surface finish; consequently, a more extensive measurement campaign is recommended to optimize and generalize the calibration of η.

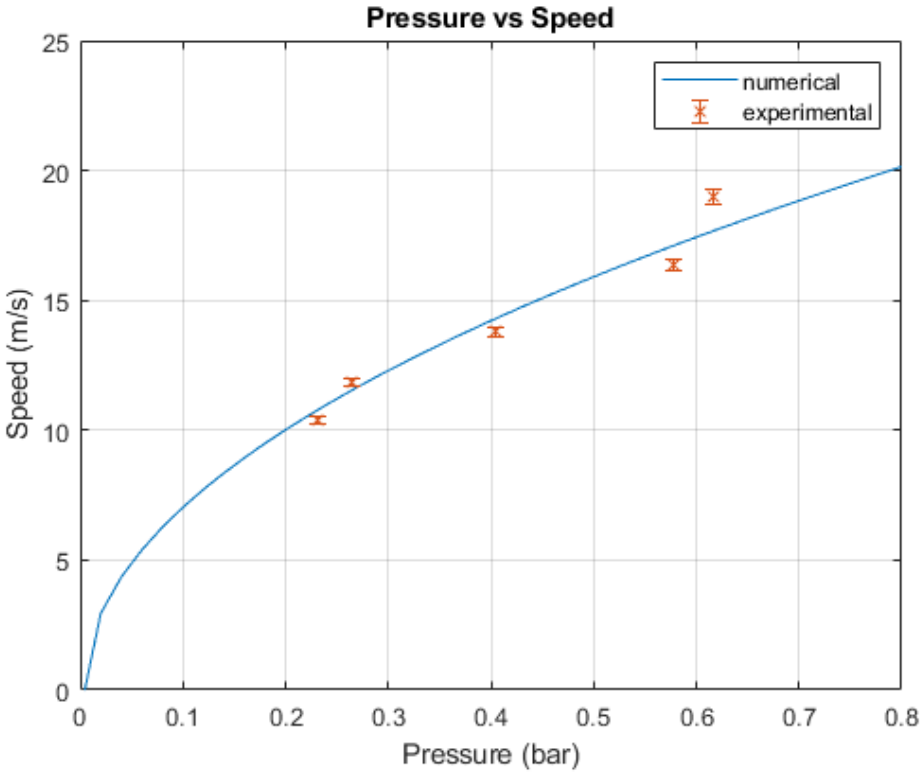

Fig. 5.2 Comparison of numerical velocity model and actual measurements

5.2 Contact force estimation

The results of the optimized contact time an force predicting models are integrated to reconstruct the complete contact pulse in the time domain. This reconstruction is achieved using the `csaps` function, as illustrated in Figure 4.9.

To evaluate the performance of the prediction pipeline, the reconstructed signals are compared to the experimentally acquired pulses using a custom designed cost function. This function quantifies the distance between the predicted and actual signals by applying a Gaussian penalty that increases with both time and amplitude discrepancies. Designed to capture differences in shape and timing, this metric provides a comprehensive measure of prediction accuracy.

$$cost = \sum_{i=1}^{m} \left(1 - \exp\left(-\left[\frac{(\tau_{actual,i} - \tau_{predicted,i})^2}{2\sigma_\tau^2} + \frac{(F_{actual,i} - F_{predicted,i})^2}{2\sigma_F^2}\right]\right)\right) \tag{5.4}$$

Where:
- the subscript i signifies each element of the time and force vectors
- m is the number of elements in the vectors
- $\sigma_\tau = 0.05(\tau_{actual})$ $\sigma_F = 0.1max(F_{actual})$ are the spreads in time and force based on the standard deviations of the actual recorded data

A visual representation of this scoring function is provided in Figure 5.3 .

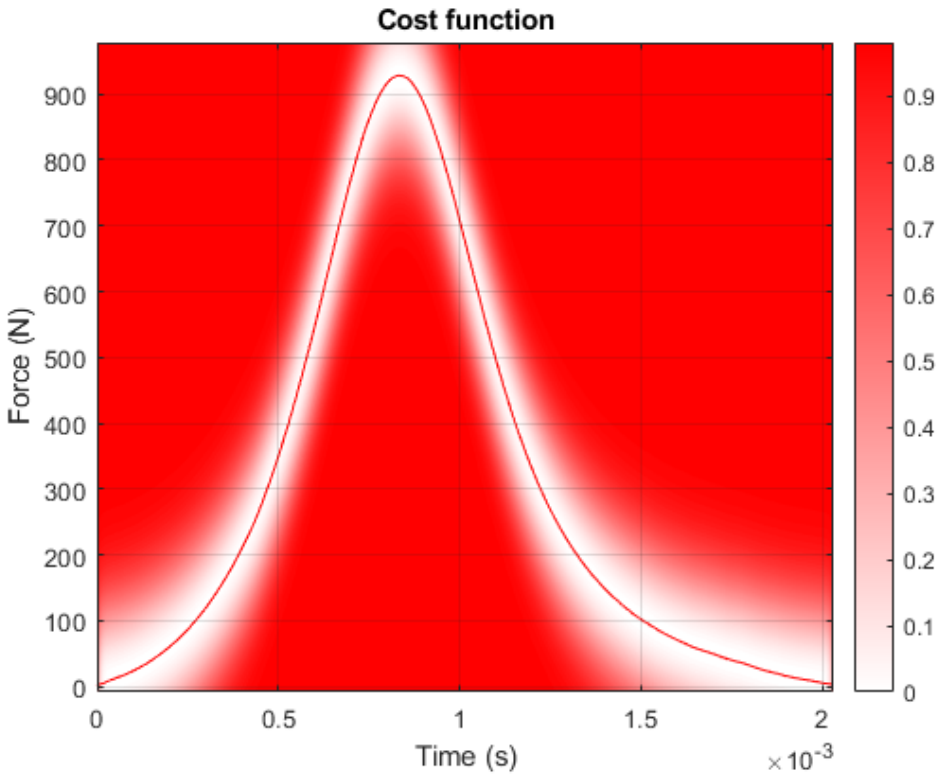

Fig. 5.3 Colormap of the proposed cost function with a generic pulse and relative tolerances.

For benchmarking purposes, the same cost function is also applied to the analytical models introduced in Chapter 1 of this thesis, allowing for a direct comparison of predictive performance across approaches. Other metrics used for evaluation are the RMSE on the force vector averaged on the entire dataset:

$$RMSE = mean\left(\sqrt{\frac{\sum_{i=1}^{n}(F - F_{interpolated})^2}{n}}\right) \tag{5.5}$$

the average error computed as in Eq. 5.6:

$$err = \frac{1}{n}\sum_{i}^{n}\frac{|\tau_{i,actual} - \tau_{i,predicted}|}{\tau_{i,actual}} \tag{5.6}$$

As shown in Table 5.2, the Gaussian Process regression delivers the most accurate overall prediction when compared to NN. This result is achieved despite a slightly higher RMSE on the force vector, thanks to a 20% lower error in the time prediction, which has a larger influence on the overall pulse shape.

It is important to underline that the errors on time prediction in Table 5.2 and Table 5.3 are exactly the same for both Reed and Hunter model since the relation used to compute contact time is the same in both cases.

Table 5.2 Mean cost value and RMSE over the entire dataset of each prediction model

Rank	**Model**	**Cost**	**Force RMSE** (N)	**Time error** (-)
1	GPy Gaussian Process	78.02	36.64	0.04
2	Neural network	125.09	35.96	0.05
3	Hann window	462.80	117.68	0.25
4	Hunter	587.58	246.63	0.27
5	Reed	611.57	421.62	0.27

A deeper insight into model behavior can be gained by examining the cost function values across all 180 tests, presented in Figure 5.4. The three analytical models, Hann, Hunter, and Reed exhibit a clear periodic degradation in accuracy. This trend corresponds to variations in the hammer tip material: predictions worsen progressively as the tip becomes softer and more energy is dissipated during impact. This behavior underlines the limitations of analytical models in capturing complex, material dependent dynamics, particularly for highly damped interactions. These observations are consistent with findings in [39], where a significant drop in accuracy was observed for polyurethane tips in coefficient of restitution (COR) estimations.

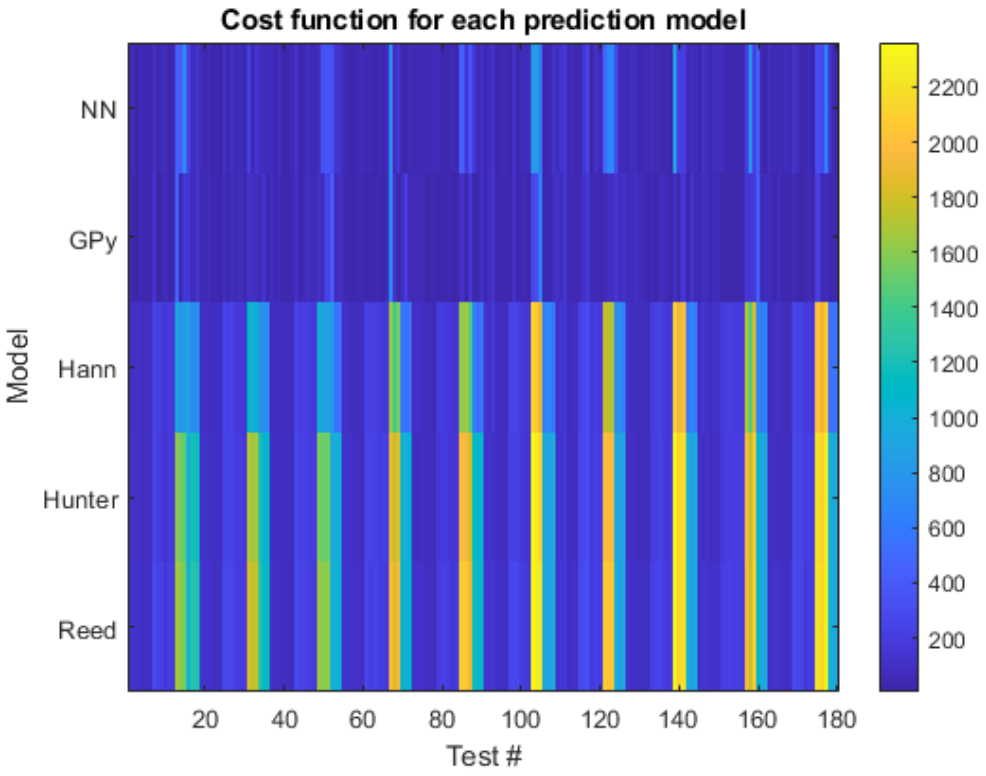

Fig. 5.4 Cost function computed for each test

To deepen the analysis, several key physical parameters were extracted from each predicted signal and compared against the corresponding ground truth values:

- Maximum Force F_{max}
- Time of Elastic phase τ_{el}
- Impulse during Elastic Compression $P_{el} = \int_0^{\tau_{el}} F(t)\,dt$
- Total Impulse over Contact Duration $P = \int_0^{\tau} F(t)\,dt$

The error on each of these four parameters is computed as:

$$error = \frac{1}{180} \cdot \sum_{i=1}^{180} \frac{|x_{actual,i} - x_i|}{x_{actual,i}} \tag{5.7}$$

where:

- $x_{actual,i}$ is the generic parameter evaluated on the acquired signal for the i^{th} test

- $x_{,i}$ is the generic parameter evaluated on the estimated signal for the i^{th} test

These metrics allow for a more physically meaningful comparison between models using parameters that are critical in contact mechanics applications.

Table 5.3 Mean errors between predictions and acquired signals on key physical parameters

Model	**Force error (-)**	τ_e **error (-)**	P **error (-)**	P_{el} **error (-)**
Neural network	0.0499	0.0628	0.0480	0.0474
GPy Gaussian Process	0.0518	0.0562	0.0308	0.0328
Hann window	0.2578	0.1828	0.1112	0.0237
Hunter	0.5224	0.2598	0.5403	0.5144
Reed	0.8153	0.2598	1.0793	1.1440

The physical parameter comparison in Table 5.3 further reinforces the trends observed in the scoring analysis. A brief evaluation of each model is presented below to summarize its predictive strengths and limitations:

The **Neural Network** model demonstrates excellent predictive performance, achieving the lowest RMSE in force reconstruction and the lowest error on maximum force estimate while also maintaining consistent physical plausibility across all evaluated parameters. Its only slight drawback lies in a marginally higher error in estimating the elastic contact time compared to the GPy model. Nonetheless, it offers reliable overall behavior and strong generalization across the dataset.

The **GPy Gaussian Process** model stands out as the best performing approach overall. While its force RMSE is slightly higher than that of the neural network, it compensates with the lowest custom cost and the most accurate prediction of the elastic contact phase duration, which plays a dominant role in shaping the contact pulse. Moreover, it maintains excellent physical consistency across all derived quantities, especially over impulse computation.

While both the gaussian process model and the NN demonstrate good predictive capabilities, they share a common limitation: the need for a large and diverse dataset to ensure proper training and validation. This requirement can pose challenges in scenarios where data collection is costly or time-consuming. Despite this, once trained, both models offer robust and reliable predictions.

The **Hann Window** model shows intermediate performance. While it performs significantly worse than the data-driven models in terms of RMSE and cost figure, it still captures the overall shape of the signal better than the other analytical models. Its physical indicators, particularly the impulse over elastic contact time, is close to reality, but since the error on the overall impulse is high that means that the majority of the error is over the restitution phase where, according to Gugan and Cross [24, 25] the majority of dissipation occurs.

The **Hunter** model performs poorly, with large errors in both force prediction and elastic contact time estimation. It also significantly overestimates all physical quantities, indicating a tendency to misrepresent the energy dissipation in the actual system.

Finally, the **Reed** model yields the least accurate predictions. It consistently produces the highest errors across all evaluation metrics, and its physical predictions, particularly impulse and power are largely unphysical. This suggests a strong mismatch between the model assumptions and the dynamics of the experimental system.

Looking at error on impulse for each of the 180 tests (Figure 5.5) it is clear how overall the best accuracy and the best consistency across all testing condition is obtained by the Gaussian Regression Model with a mean error on the validation set of 3.08 % and a maximum of just 25 % as an outlier.

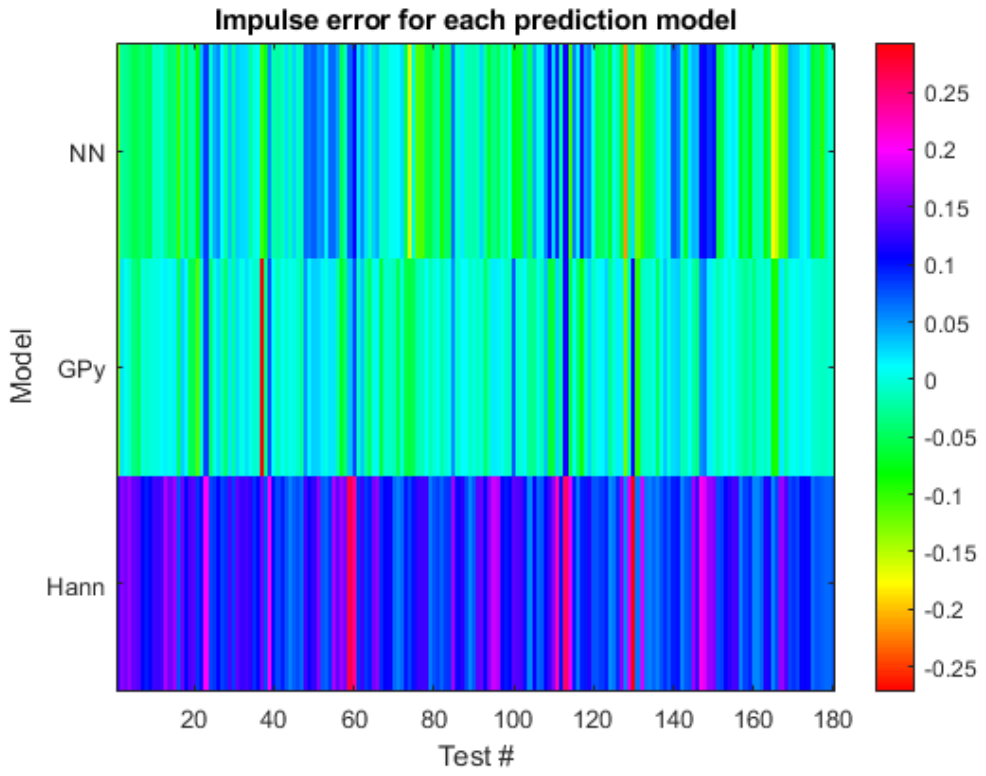

Fig. 5.5 Error on impulse of each test

In conclusion, among all the models evaluated, the Gaussian Process regression model is the most accurate and physically consistent approach for predicting contact forces and durations. It delivers the lowest overall cost value, maintains low error levels across all key physical parameters, and exhibits robust performance across a wide range of test conditions. While the neural network also demonstrates strong performance, especially in force prediction, the Gaussian Process model's superior accuracy in impulse make it the most suitable choice for modeling impact dynamics in this study.

Chapter 6

Conclusions

This work set out to advance the understanding of impact induced contact forces in pyroshock events and to complete the commissioning of the Politecnico di Torino resonant plate test bench. By coupling a data-driven and numerical modelling all three initial objectives have been achieved, as summarized below.

- **Development of a data-driven contact force model**
  A machine learning algorithm has been trained and validated on an extensive hammer impact database, enabling accurate reconstruction of the contact force time history. This model consistently outperformed analytical methods in RMSE but also in all key parameters such as the peak force, impulse and elastic contact time across variations in impact velocity, geometry, and material properties of the contacting bodies. This will allow a reduction in calibration tests reducing the associated costs.
  Moreover, the framework generalizes beyond pyroshock applications, providing a modular foundation for a contact force digital twin adaptable to diverse engineering scenarios, furthering the state of the art of continuous contact mechanics.

- **Design and Implementation of the experimental setup**
  A resonant plate test bench was finalized, featuring an adjustable free-free suspension where all critical components guarantee a safety factor higher than 3.9 under dynamic loading conditions. The projectiles have been designed in such a way to allow rapid changes in geometry and mechanical properties of the tip.

The plate and the pneumatic gun have been instrumented with a robust measurement chain, that allows to capture the response of the plate, but also acquisition of each parameter that influences the contact between the projectile and the resonant fixture.
This setup lays a versatile platform for systematic contact mechanics studies and pyroshock qualification tests.

- **Validation of the projectile velocity prediction**
  An adiabatic expansion model of the pneumatic gun, based on tank volume, barrel geometry and friction losses was implemented in MATLAB and benchmarked against low pressure firing. Introducing a correction for blow by leakages, predicted muzzle velocities agreed within 4% of the measured values on average, confirming the digital twin capability of reducing down time associated with calibration.

At the same time, some limitations can be found. Despite its robust performance, the data-driven contact force model was trained using only a single hammer mass, which may lead to unreliable predictions when projectiles of substantially different weight are employed. Likewise, impacts involving aluminum tips, characterized by very brief contact durations, are represented by a low number of sample due to low sampling frequency. FInally the model black-box nature: although it reproduces force waveforms with high fidelity, it offers limited physical insight into how variations in mass, velocity, or stiffness interact to shape the contact pulse.

On the experimental side, the chain based height adjustment system, while mechanically simple and strong, permits only discrete suspension increments, which can reduce fine tuning. Between shots, extracting the projectile from the barrel requires a long time since it has to be done using very low pressure, slowing test throughput.

Finally, although the adiabatic-expansion model of the pneumatic gun predicts muzzle velocity within 4 % of measured values, its reliance on an empirical blow by correction coefficient necessitates a new calibration campaign whenever projectile diameter changes partially offsetting the downtime savings.

6.1 Future directions

Several avenues exist to extend and deepen the present study: The data-driven prediction algorithm demonstrates strong accuracy, but its generalizability would benefit from a larger, more diverse set of pneumatic gun impacts involving more materials, geometries and boundary conditions.

Furthermore, the creation of a complete dataset of pneumatic gun generated impacts, other than being beneficial to deepen the understanding of contact mechanics, could provide ground truth validation data for extreme conditions that are impossible to generate manually using a hammer.

Another area of interest is the development of a ML model capable of determining force evolution and contact duration in a single passage potentially using physics-based data-driven hybrids modeling methods, allowing to streamline the prediction workflow and remove any error that can arise with signal reconstruction.

Finally even if the velocity predicting model is already capable to produce estimates with very good accuracy a more comprehensive validation using tests that span over different materials and over the entire range of pressure that the gun can produce could lead to better understanding on the losses that in this work are not accounted for.

For what concerns the experimental set up the use of a pneumatic valve increases the complexity of the pneumatic circuit and reduces the ease of opening time control and actuation. An electrically actuated valve would remove the need for a two branch pneumatic circuit and programmable discharge timing would enable parametric studies of valve opening profiles on muzzle velocity..

Finally, the creation of a soft material sabot for the bullet would allow to increase the efficiency in energy conversion from the potential energy of the compressed air to the kinetic energy of the bullet, ultimately allowing for higher energy impacts if needed.

Appendix A

Latin Hypercube Sampling Dataset

This appendix presents the full set of parameters for each of the 105 tests generated using Latin Hypercube Sampling, as explained in Chapter 3. To enhance the statistical robustness of the dataset, each test configuration is repeated 10 times, resulting in a total of 1050 recorded impact events.

The test matrix is inherently randomized due to LHS design, this minimize the influence of systematic biases, such as operator fatigue or other time dependent variable that could otherwise affect data consistency across long acquisition sessions, but setup time increases whenever hardware changes are required. In particular, swapping resonant plates, using shop cranes or hydraulic hoists, is both time consuming and poses safety risks. To minimize these hazards and reduce downtime, plate material, anvil material, and insulator type are not randomized.

Throughout the experimental campaign, data integrity must be carefully monitored. It is essential to ensure that no acquisition channel exceeds its bandwidth limitations, and that any corrupted or incomplete recordings are promptly identified and discarded. These precautions are crucial to maintaining a consistent and reliable dataset suitable for training and validating data-driven models.

Table A.1 LHS Design of Experiments

#	*Plate Material*	*Anvil Plate*	*Insulator*	*Bullet Tip*	*Radius (mm)*	*Mass (kg)*	*Bullet velocity*
1	aluminum	none	none	PLA	30.00	1.00	High
2	aluminum	none	none	aluminum	30.00	1.00	Low
3	aluminum	none	none	steel	30.00	0.20	Low
4	aluminum	none	none	PLA	45.00	0.20	High
5	aluminum	none	none	PLA	45.00	0.50	Medium
6	aluminum	none	none	steel	30.00	1.00	Medium
7	aluminum	none	none	PLA	30.00	0.50	Low
8	aluminum	none	none	PLA	30.00	0.20	Low
9	aluminum	none	none	steel	45.00	0.20	Medium
10	aluminum	none	none	steel	30.00	1.00	High
11	aluminum	none	none	aluminum	30.00	1.00	Medium
12	aluminum	aluminum	none	PLA	45.00	1.00	High
13	aluminum	aluminum	none	aluminum	45.00	0.20	High
14	aluminum	aluminum	none	steel	60.00	1.00	High
15	aluminum	aluminum	none	steel	30.00	0.50	High
16	aluminum	aluminum	none	aluminum	45.00	0.20	Medium
17	aluminum	aluminum	none	aluminum	30.00	0.20	Low
18	aluminum	aluminum	none	steel	45.00	1.00	Medium
19	aluminum	aluminum	none	aluminum	45.00	1.00	Low
20	aluminum	aluminum	none	aluminum	60.00	0.20	High
21	aluminum	aluminum	none	aluminum	45.00	0.20	High
22	aluminum	aluminum	none	PLA	30.00	1.00	Medium
23	aluminum	aluminum	none	PLA	45.00	0.20	Medium
24	aluminum	aluminum	polymeric	PLA	60.00	0.20	Low
25	aluminum	aluminum	polymeric	PLA	60.00	1.00	Medium
26	aluminum	aluminum	polymeric	steel	45.00	1.00	Low
27	aluminum	aluminum	polymeric	aluminum	45.00	1.00	Medium
28	aluminum	aluminum	polymeric	steel	30.00	0.50	Low

#	*Plate Material*	*Anvil Plate*	*Insulator*	*Bullet Tip*	*Radius (mm)*	*Mass (kg)*	*Bullet velocity*
29	aluminum	aluminum	polymeric	aluminum	30.00	0.50	Low
30	aluminum	aluminum	polymeric	steel	45.00	0.20	Medium
31	aluminum	aluminum	polymeric	steel	60.00	1.00	Medium
32	aluminum	aluminum	polymeric	PLA	60.00	0.50	High
33	aluminum	aluminum	polymeric	PLA	45.00	1.00	Medium
34	aluminum	aluminum	polymeric	PLA	60.00	0.50	High
35	aluminum	steel	none	PLA	45.00	0.20	High
36	aluminum	steel	none	PLA	45.00	0.50	Medium
37	aluminum	steel	none	PLA	30.00	1.00	Low
38	aluminum	steel	none	aluminum	45.00	0.50	Medium
39	aluminum	steel	none	aluminum	30.00	1.00	Medium
40	aluminum	steel	none	aluminum	30.00	1.00	Low
41	aluminum	steel	none	aluminum	30.00	1.00	High
42	aluminum	steel	none	aluminum	60.00	1.00	Medium
43	aluminum	steel	none	steel	30.00	1.00	Low
44	aluminum	steel	none	PLA	45.00	0.20	Low
45	aluminum	steel	none	PLA	60.00	1.00	Medium
46	aluminum	steel	none	steel	60.00	0.50	High
47	aluminum	steel	none	aluminum	60.00	0.50	Low
48	aluminum	steel	polymeric	PLA	45.00	0.50	High
49	aluminum	steel	polymeric	steel	45.00	1.00	Low
50	aluminum	steel	polymeric	PLA	60.00	0.20	Low
51	aluminum	steel	polymeric	PLA	45.00	0.20	Low
52	aluminum	steel	polymeric	aluminum	60.00	1.00	Low
53	aluminum	steel	polymeric	aluminum	30.00	0.50	High
54	aluminum	steel	polymeric	aluminum	60.00	0.50	High
55	aluminum	steel	polymeric	aluminum	60.00	1.00	Medium
56	aluminum	steel	polymeric	aluminum	60.00	0.50	High
57	aluminum	steel	polymeric	PLA	60.00	1.00	Medium
58	aluminum	steel	polymeric	PLA	60.00	0.20	High

#	*Plate Material*	*Anvil Plate*	*Insulator*	*Bullet Tip*	*Radius (mm)*	*Mass (kg)*	*Bullet velocity*
59	aluminum	steel	polymeric	steel	60.00	0.20	Medium
60	aluminum	steel	polymeric	PLA	30.00	0.20	Low
61	aluminum	steel	polymeric	PLA	60.00	0.50	Medium
62	aluminum	steel	polymeric	PLA	30.00	0.20	High
63	aluminum	steel	polymeric	steel	45.00	1.00	Medium
64	aluminum	steel	polymeric	aluminum	60.00	1.00	High
65	aluminum	steel	polymeric	steel	45.00	1.00	Medium
66	steel	none	none	steel	60.00	0.20	Low
67	steel	none	none	PLA	30.00	0.50	Low
68	steel	none	none	aluminum	45.00	0.20	Low
69	steel	none	none	aluminum	30.00	1.00	High
70	steel	none	none	aluminum	45.00	0.50	Medium
71	steel	none	none	steel	30.00	0.50	Low
72	steel	none	none	PLA	60.00	0.50	Medium
73	steel	none	none	aluminum	30.00	0.50	Low
74	steel	none	none	PLA	45.00	0.50	High
75	steel	none	none	aluminum	30.00	0.20	Low
76	steel	none	none	steel	30.00	0.50	High
77	steel	none	none	PLA	60.00	0.20	Low
78	steel	none	none	PLA	60.00	0.50	Medium
79	steel	none	none	steel	30.00	0.20	Low
80	steel	none	none	aluminum	60.00	0.50	Low
81	steel	none	none	steel	60.00	1.00	Medium
82	steel	aluminum	none	aluminum	45.00	1.00	Low
83	steel	aluminum	none	steel	30.00	0.50	Low
84	steel	aluminum	none	steel	30.00	0.50	Medium
85	steel	aluminum	none	steel	30.00	1.00	High
86	steel	aluminum	none	steel	60.00	0.50	Low
87	steel	aluminum	none	steel	30.00	0.50	High
88	steel	aluminum	none	aluminum	60.00	1.00	Medium

#	*Plate Material*	*Anvil Plate*	*Insulator*	*Bullet Tip*	*Radius (mm)*	*Mass (kg)*	*Bullet velocity*
89	steel	aluminum	none	steel	45.00	0.50	High
90	steel	aluminum	none	aluminum	60.00	0.20	High
91	steel	aluminum	none	aluminum	45.00	0.50	High
92	steel	aluminum	none	steel	45.00	0.50	Low
93	steel	aluminum	none	steel	45.00	0.20	Medium
94	steel	aluminum	none	aluminum	60.00	0.20	High
95	steel	aluminum	none	steel	60.00	0.50	High
96	steel	aluminum	polymeric	steel	60.00	0.50	Low
97	steel	aluminum	polymeric	steel	45.00	0.20	Medium
98	steel	aluminum	polymeric	PLA	60.00	0.20	Medium
99	steel	aluminum	polymeric	steel	45.00	0.50	Medium
100	steel	aluminum	polymeric	steel	45.00	0.20	Low
101	steel	aluminum	polymeric	steel	30.00	0.20	High
102	steel	aluminum	polymeric	PLA	45.00	0.50	High
103	steel	aluminum	polymeric	aluminum	30.00	1.00	High
104	steel	aluminum	polymeric	PLA	45.00	0.50	High
105	steel	aluminum	polymeric	aluminum	45.00	1.00	High

References

[1] C. J. Moening. Pyroshock flight failures. In *Proceedings of 31st Annual Technical Meeting of the Institute of Environmental Sciences*, May 1985.

[2] NASA. Nasa technical standard: Pyroshock testing. Technical Report NASA-STD-7003, National Aeronautics and Space Administration (NASA), March 2003.

[3] International Organization for Standardization. Mechanical vibration and shock — Signal processing, 2007. ISO Standard No. 18431-4:2007.

[4] Luca Viale. *Pyroshock Testing: A Theoretical and Experimental Investigation for the Qualification of Aerospace Equipment*. Ph.d. dissertation, Politecnico di Torino, Turin, Italy.

[5] Juho Lee, Dae-Hyun Hwang, Jae-Kyeong Jang, Dong-Jin Kim, YeungJo Lee, Jung-Ryul Lee, and Jae-Hung Han. Pyroshock prediction of ridge-cut explosive bolts using hydrocodes. *Shock and Vibration*, 2016(1):1218767, 2016.

[6] Shihui Xiong, Yanhua Li, Yaokun Ye, Jingcheng Wang, Huina Mu, and Yuquan Wen. Quantitatively decoupling the impact of preload and internal mechanism motion on pyrotechnic separation shock. *International Journal of Aeronautical and Space Sciences*, 22(5):1106–1117, 2021.

[7] Jung-Ryul Lee, Chen Ciang Chia, and Churl-Won Kong. Review of pyroshock wave measurement and simulation for space systems. *Measurement*, 45(4):631–642, 2012.

[8] NASA. Dynamic environmental criteria: Nasa technical handbook. Technical Report NASA-HDBK-7005, National Aeronautics and Space Administration (NASA), March 2001.

[9] Abdulla Almesmari, Firas Jarrar, Fahad Almaskari, Prashanth R Marpu, Nellimala Abdul Shukoor, and Jinumon K Govindan. Development of a metal-to-metal mid-field shock test procedure for nanosatellites. *IEEE Journal on Miniaturization for Air and Space Systems*, 1(2):103–109, 2020.

[10] Stefan Kiryenko, Gaetan Piret, and Jan Kasper. Esa/estec shock bench presentation. In *Spacecraft Structures, Materials and Mechanical Testing 2005*, volume 581, 2005.

[11] B Charvet, D Dilhan, and M Palladino. Shock bench enhancements. In *13th European Conference on Spacecraft Structures, Materials & Environmental Testing*, volume 727, page 98, 2014.

[12] Sandia National Laboratories, Validation and Qualification Sciences Experimental Complex (VQSEC). Mechanical shock complex. https://www.sandia.gov/vqsec/facilities/mechshock/, 2025. Accessed May 20, 2025.

[13] U von Wagner, N Jüngel, S Ritzmann, A Bäger, and Albert Einstein-Str. Simulation of pyroshocks. In *Proceedings of the 1st CEAS European Air and Space Conference, Berlin, Germany*, pages 10–13, 2007.

[14] Wonki Bae and Junhong Park. Optimization of pyroshock test conditions for aerospace components to enhance repeatability by genetic algorithms. *Aerospace*, 11(9):700, 2024.

[15] Unholtz-Dickie Corp. (UDCO). T2000 series induct-a-ring electrodynamic shaker systems. https://www.udco.com/products/electrodynamic-shaker-systems/t-series/shaker-t2000/, 2025. Accessed June 8, 2025.

[16] G. Gilardi and I. Sharf. Literature survey of contact dynamics modelling. *Mechanism and machine theory*, 37(10):1213–1239, 2002.

[17] W.J. Stronge. *Impact mechanics / W.J. Stronge*. CUP, Cambridge, 2000.

[18] E. T. 1873-1956 Whittaker. *A treatise on the analytical dynamics of particles and rigid bodies; with an introduction to the problem of three bodies / By E. T. Whittaker*. University press, 1904, Massachusetts, 1904.

[19] 1831-1907 Routh, Edward John. *The elementary part of A treatise on the dynamics of a system of rigid bodies*. Macmillan and co.,limited, 1905, England, 1905.

[20] C.T. Lim and W.J. Stronge. Oblique elastic–plastic impact between rough cylinders in plane strain. *International journal of engineering science*, 37(1):97–122, 1999.

[21] Clarence Zener. The intrinsic inelasticity of large plates. *Physical review*, 59(8):669–673, 1941.

[22] Graham Weir and Stephen Tallon. The coefficient of restitution for normal incident, low velocity particle impacts. *Chemical Engineering Science*, 60(13):3637–3647, 2005.

[23] Deepak Patil and C Fred Higgs. Experimental investigations on the coefficient of restitution for sphere–thin plate elastoplastic impact. *Journal of tribology*, 140(1), 2018.

[24] D. Gugan. Inelastic collision and the hertz theory of impact. *American Journal of Physics - AMER J PHYS*, 68:920–924, 10 2000.

[25] Rod Cross. The bounce of a ball. *American Journal of Physics - AMER J PHYS*, 67:222–227, 03 1999.

[26] Kenneth Hunt and Erskine Crossley. Coefficient of restitution interpreted as damping in vibroimpact. *Journal of applied mechanics*, 1975.

[27] Mariana Rodrigues da Silva, Filipe Marques, Miguel Tavares da Silva, and Paulo Flores. A compendium of contact force models inspired by hunt and crossley's cornerstone work. *Mechanism and Machine Theory*, 167:104501, 2022.

[28] Gregory C. McLaskey and Steven D. Glaser. Hertzian impact: Experimental study of the force pulse and resulting stress waves. *The Journal of the Acoustical Society of America*, 128(3):1087–1096, 2010.

[29] Kyle Hickmann, Deborah Shutt, Andrew K Robinson, and Jonathan Lind. Data-driven learning of impactor strength properties from shock experiments with additively manufactured materials. In *Applications of Machine Learning 2021*, volume 11843, page 1184303. SPIE, 2021.

[30] Samuel Thompson. *Using machine learning to predict the ballistic response of structures to projectile impact*. PhD thesis, University of Edinburgh, 2023.

[31] Zhymir Thompson, Austin RJ Downey, Jason D Bakos, Jie Wei, and Jacob Dodson. Multi-modal generative adversarial networks for synthesizing time-series structural impact responses. *Mechanical Systems and Signal Processing*, 204:110725, 2023.

[32] Johannes Reiner, Reza Vaziri, and Navid Zobeiry. Machine learning assisted characterisation and simulation of compressive damage in composite laminates. *Composite Structures*, 273:114290, 2021.

[33] Jingyu Zhao, Ben Wang, Qihui Lyu, Weihua Xie, Zaoyang Guo, and Bing Wang. Compression after multiple impact strength of composite laminates prediction method based on machine learning approach. *Aerospace Science and Technology*, 136:108243, 2023.

[34] Qian Liu, Jianxun Liang, and Ou Ma. A physics-based and data-driven hybrid modeling method for accurately simulating complex contact phenomenon. *Multibody System Dynamics*, 50(1):97–117, 2020.

[35] Federico Pavone. Test bench design and contact model analysis for pyroshock testing, 2024.

[36] Paul J Hazell. *Armour: materials, theory, and design*. CRC press, 2022.

[37] Jien Nishiwaki. Resistance to the penetration of a bullet through an aluminium plate. *Journal of the Physical Society of Japan*, 6(5):374–378, 1951.

[38] R F Bishop, R Hill, and N F Mott. The theory of indentation and hardness tests. *Proceedings of the Physical Society*, 57(3):147, may 1945.

[39] Luca Viale and Gunnar Tibert. Description and analysis of a full factorial open-access dataset for aerospace shock testing. Manuscript under review at Mechanical Systems and Signal Processing, 2025.

[40] Kistler Group. Piezoelectric ring force transducers for tensile and compression forces from 20 kn to 700 kn. Product data sheet.

[41] Uni en 1993-1-8:2005/ac:2005 - eurocode 3: Design of steel structures - part 1-8: Design of joints. https://store.uni.com/uni-en-1993-1-8-2005, 2005.

[42] Vdi 2230 part 1: Systematic calculation of highly stressed bolted joints — joints with one cylindrical bolt. https://www.vdi.de/en/home/vdi-standards/details/vdi-2230-blatt-1-systematic-calculation-of-highly-stressed-bolted-joints-joints-with-one-cylindrica 2014.

[43] Luisa F. Cabeza. *Encyclopedia of Energy Storage*, volume 1, page 29. Elsevier, Amsterdam, Netherland, 2022.

[44] A Cave, S Roslyakov, M Iskander, and S Bless. Design and performance of a laboratory pneumatic gun for soil ballistic applications. *Experimental Techniques*, 40:541–553, 2016.

[45] Jiju. Antony. *Design of experiments for engineers and scientists*. Butterworth-Heinemann, Oxford, 1st ed. edition, 2003.

[46] Xenia Yasmin Ratke and Thomas Sattel. Thermal characterization, modeling and parametric model order reduction (pmor) of piezoelectric transducers. *Smart Materials and Structures*, 2025.

[47] Younhee Choi, Doosam Song, Sungmin Yoon, and Junemo Koo. Comparison of factorial and latin hypercube sampling designs for meta-models of building heating and cooling loads. *Energies*, 14(2):512, 2021.

[48] Jason L Loeppky, Jerome Sacks, and William J Welch. Choosing the sample size of a computer experiment: A practical guide. *Technometrics*, 51(4):366–376, 2009.

[49] Arshad Afzal, Kwang-Yong Kim, and Jae-won Seo. Effects of latin hypercube sampling on surrogate modeling and optimization. *International Journal of Fluid Machinery and Systems*, 10(3):240–253, 2017.

[50] Felipe AC Viana. A tutorial on latin hypercube design of experiments. *Quality and reliability engineering international*, 32(5):1975–1985, 2016.

[51] ANSYS, Inc. ANSYS Granta Materials Data. Accessed via Granta EduPack 2021 R2, 2021. Material properties database provided by ANSYS Granta. Available at: https://www.ansys.com/it-it/products/materials/granta-edupack.

[52] Chapter 2 wave propagation and impact. In Jonas A. Zukas, editor, *Introduction to Hydrocodes*, volume 49 of *Studies in Applied Mechanics*, pages 33–74. Elsevier, 2004.

[53] Djordje Slijepcevic and Horst. Explaining machine learning models for clinical gait analysis. *ACM Transactions on Computing for Healthcare (HEALTH)*, 3(2):1–27, 2021.

[54] Aleksei Krotov, Reza Sharif Razavian, Mohsen Sadeghi, and Dagmar Sternad. Time-warping analysis for biological signals: methodology and application. *Scientific Reports*, 15(1):11718, 2025.

[55] T. Hastie, R. Tibshirani, and J.H. Friedman. *The Elements of Statistical Learning: Data Mining, Inference, and Prediction*. Springer series in statistics. Springer, 2009.

[56] The MathWorks Inc. Partial Least Squares. Accessed on 2025-03-18. Available at: https://it.mathworks.com/help/stats/partial-least-squares.html.

[57] Jianming Hu and Jianzhou Wang. Short-term wind speed prediction using empirical wavelet transform and gaussian process regression. *Energy (Oxford)*, 93:1456–1466, 2015.

[58] Le Zhou, Zhihuan Song, Junghui Chen, and Gang Li. Recursive gaussian process regression model for adaptive quality monitoring in batch processes. *Mathematical problems in engineering*, 2015(2015):1–9, 2015.

[59] G.Peter Zhang, B.Eddy Patuwo, and Michael Y. Hu. A simulation study of artificial neural networks for nonlinear time-series forecasting. *Computers operations research*, 28(4):381–396, 2001.

[60] Xavier Glorot, Antoine Bordes, and Y. Bengio. Deep sparse rectifier neural networks. volume 15, 01 2010.

[61] Tomasz Szandała. Review and comparison of commonly used activation functions for deep neural networks. In *Bio-inspired neurocomputing*, pages 203–224. Springer, 2020.

[62] Akhilesh A. Waoo and Brijesh K. Soni. Performance analysis of sigmoid and relu activation functions in deep neural network. In Amit Sheth, Amit Sinhal, Abhinav Shrivastava, and Amit Kumar Pandey, editors, *Intelligent Systems*, pages 39–52, Singapore, 2021. Springer Singapore.

[63] Jiawei Tang, Xiaowen Lin, Fei Zhao, and Xi Chen. Industrial data modeling with low-dimensional inputs and high-dimensional outputs. *IEEE Transactions on Industrial Informatics*, 20(1):835–844, 2023.

[64] Jiawei Tang, Xiaowen Lin, Fei Zhao, and Xi Chen. Low-dimensional input and high-dimensional output modelling using gaussian process. In *Computer Aided Chemical Engineering*, volume 49, pages 1639–1644. Elsevier, 2022.

[65] Gpytorch library. https://gpytorch.ai/.

[66] Hussain Alibrahim and Simone A. Ludwig. Hyperparameter optimization: Comparing genetic algorithm against grid search and bayesian optimization. In *2021 IEEE Congress on Evolutionary Computation (CEC)*, pages 1551–1559. IEEE, 2021.

[67] JCGM Jcgm et al. Evaluation of measurement data—guide to the expression of uncertainty in measurement. *Int. Organ. Stand. Geneva ISBN*, 50:134, 2008.

[68] J. Corner. The internal ballistics of a leaking gun. *Proceedings of the Royal Society A*, 188:237–255, 1946. Communicated by N. F. Mott, F.R.S. Received 4 April 1946.